Research Paper

Heat transfer enhancement of water-cooled triply periodic minimal surface heat exchangers

Wenguang Li [a], Weihong Li [b], Zhibin Yu [a],*

[a] School of Engineering, University of Glasgow, G12 8QQ Glasgow, UK
[b] Department of Mechanical Engineering, City University of Hong Kong, Kowloon Tong, Hong Kong, China

ARTICLE INFO

ABSTRACT

Whether triply periodic minimal surface (TPMS) heat exchangers are applicable to cooling or cold storage systems as a cooler for supercritical carbon dioxide (SCO2) is undocumented. Here the conjugated heat transfer of SCO2 in TPMS Schoen-G heat exchanger and printed circuit heat exchanger (PCHE) was predicted based on three-dimensional steady turbulent Reynolds-averaged Navier-Stokes equations, energy equation and shear stress transport model using computational fluid dynamics software ANSYS CFX when SCO2 inlet temperature and pressure vary in 65–30 °C and (8–9)MPa. SCO2 in two heat exchangers is cooled under counter-flow conditions by a stream of cold water with given inlet temperature and mass flow rate. It was shown that the mean heat transfer coefficient of SCO2 in TPMS Schoen-G heat exchanger is larger than PCHE. As the inlet pressure rises, the friction factor increases and Nusselt number decreases in the heat exchangers due to decreased Reynolds number and Prandtl number, respectively. The friction factor ratio, Nusselt number ratio and performance evaluation criterion vary in the range of 0.38–0.50, 1.07–1.49, and 1.45–2.04 with Reynolds number and inlet temperature when the PCHE serves as a reference heat exchanger. The streamlines in TPMS Schoen-G heat exchanger are quite smooth even though the areas with a higher velocity appear. The streamlines in PCHE exhibit a spiral flow pattern to result in extra hydraulic loss. The heat transfer enhancement of TPMS Schoen-G heat exchanger is much better TPMS Schwarz-D heat exchanger at a Reynolds number higher than 16,000. The enhancement is attributed to a larger heat transfer surface area and more topological tortuosity without flow separation than PCHE.

1. Introduction

Triply periodic minimal surface (TPMS) structures are composed of two distinct interpenetrating volume domains separated by a wall with minimal area. TPMS divides a three-dimensional (3D) space into two interpenetrating channels to create a large surface area-to-volume ratio. TPMS can be found in nature, e.g., in biological membranes, rock crystals, and co-polymer phases as inter-material dividing surfaces. TPMS structures can demonstrate excellent structural strength with minimal material usage and can enhance heat transfer over micro-channel heat exchangers by a factor of 10–100. TPMS structures have been applied to heat exchangers [1], static mixers [2], mass transfer packing [3], heatsinks [4], porous media [5] and tissue engineering scaffold [6], and a brief review of TPMS structures and applications is provided in Appendix A.

In 2011, a method of using TPMS or a minimal TPMS skeleton to make a heat exchanger component was proposed and the steps of the method for making heat exchanger components were also provided in the patent document [7]. TPMS heat exchangers with geometries Schwarz-D, Schoen-IWP, Schoen-G and Schwarz-P were fabricated, and their thermal and hydraulic performance was tested. The heat exchanger with TPMS Schwarz-D structure showed the best heat transfer characteristics with respect to inherent pressure drop in laminar flow regime [8]. TPMS structures were used to design advanced heat exchangers for SCO2 Brayton power cycles. A TPMS heat exchanger for SCO2 Brayton power cycles was fabricated with 3D printing technique. The thermal and hydraulic performance was predicted with computational fluid dynamics (CFD) method to identify the most promising geometries with high heat transfer coefficients and compactness. The fluid flow and heat transport equations are solved using finite volume method. The tortuous passages in the TPMS heat exchanger enhanced the convective heat transfer of the fluids by increased surface area, thereby the efficiency of the heat exchanger was improved [9]. A heat exchanger with TPMS

---

* Corresponding author.
E-mail addresses: Wenguang.Li@glasgow.ac.uk (W. Li), weihongli6@cityu.edu.hk (W. Li), Zhibin.Yu@glasgow.ac.uk (Z. Yu).

Nomenclature

a	constant in the μ_t expression of the shear stress transport model, $a = 0.31$
A	overall heat exchange area in a heat exchanger, m^2
B	constant in log-law velocity profile, $B=5.2$ for hydraulically smooth walls
C_p	specific heat capacity of fluid, J/kg
C_{pb}	bulk mean specific heat capacity of fluid, J/kg
c	constant in Eq. (17)
d_h	hydraulic diameter, mm
f	Darcy–Weisbach friction factor of TPMS heat exchanger
f_0	Darcy–Weisbach friction factor of reference heat exchanger
F_1	blending function between the Wilcox k-ω model and the standard k-ε model
F_2	auxiliary variable in the μ_t expression of the shear stress transport model
G	mass flux, $kg/m^2\,s$
h	specific enthalpy of fluid, m^2/s^2
k	turbulence kinetic energy, m^2/s^2
m_f	mass flow rate of cold-water, kg/s
Nu	Nusselt number of TPMS heat exchanger
Nu_0	Nusselt number of reference heat exchanger
p	fluid static pressure, Pa or MPa
$P_{kb}, P_{\omega b}$	buoyancy production term in the k- and ω-equations, respectively, J/m^3
Pr	fluid Prandtl number
Pr_t	turbulent Prandtl number, $Pr_t=0.9$
q_w	water heat flux across the tube wall, kW/m^2
Re	Reynolds number at the inlet of tube
S_E	source term of energy equation, J/m^3
S_i	specific body force, $i=1, 2, 3$, m/s^2
T	local temperature of fluid, K or ℃
T_1	fluid temperature at inlet of the tube, K or ℃
T_b	mean bulk temperature of fluid, K or ℃
T_c	temperature at pseudo critical point of fluid, K or ℃
T_n	fluid temperature in the first mesh layer, K or ℃
T_s	cross-sectional mean temperature of SCO2 or metal sheet or cold-water, K
T_w	mean wall temperature, K or ℃
T^+	dimensionless temperature in the boundary layer
u_b	bulk velocity of SCO2 in the hot side of heat exchanger, m/s
u_i, u_j	Reynolds time-averaged velocity components of fluid in a Cartesian coordinate system, $i, j=1,2, 3$, m/s
u_n	fluid velocity near wall, m/s
u_τ	friction velocity of fluid at wall, $\tau_w = \rho u_\tau^2$, m/s
u_i'	turbulent fluctuation velocity of fluid, m/s
$u_\tau^{log}, u_\tau^{vis}$	friction velocities at wall by using the solutions in the log-law and sublayer layers
U	mean heat transfer coefficient, $W/m^2 K$
x, y, z	Three Cartesian coordinates, m
x_i, x_j	coordinates of a Cartesian coordinate system, $i, j=1, 2, 3$, m
y_n	distance to the nearest wall from the first mesh layer, m
y^+	dimensionless wall distance, $y^+=\sqrt{\tau_w/\rho}\,y_n/\nu$

Greek

$\alpha_1, \beta_1, \sigma_{\omega 1}$	constants in the ω-equation of the Wilcox k-ω model, $\alpha_1=5/9$, $\beta_1=0.075$, $\sigma_{\omega 1}=2$
$\alpha_2, \beta_2, \sigma_{\omega 2}$	constants in the ω-equation of the ω-transformed standard k-ε model, $\alpha_2=0.44$, $\beta_2=0.0828$, $\sigma_{\omega 2}=1/0.856$
$\alpha_3, \beta_3, \sigma_{\omega 3}$	blended model constants in the ω-equation of the blended Wilcox k-ω and standard k-ε models, $\alpha_3=F_1\alpha_1+(1-F_1)\alpha_2$, $\beta_3=F_1\beta_1+(1-F_1)\beta_2$, $\sigma_{\omega 3}=F_1\sigma_{\omega 1}+(1-F_1)\sigma_{\omega 2}$

β	auxiliar variable in dimensionless fluid temperature expression in the boundary layer
β_k	constant in the k-equation of the Wilcox k-ω model and the ω-transformed standard k-ε model, $\beta_k=0.09$
Γ	auxiliary variable dimensionless fluid temperature in boundary layer
γ	magnitude of the strain rate of fluid velocity, 1/s
γ_{ij}	strain rate tensor of fluid velocity, 1/s
Δp	difference in the pressure of SCO2 across heat exchanger, Pa
ΔT_s	cross-sectional averaged temperature difference between SCO2 and metal sheet, K
$\Delta x, \Delta y, \Delta z$	lengths of a heat exchanger in x, y, z directions, m
δ	thickness of metal sheet in heat exchanger, mm
ε	dissipation rate of turbulence kinetic energy, m^2/s^3
ζ	specific solid–fluid interface area, 1/m
θ	zigzag angle of channels of heat exchanger, °
κ	von Kármán constant, $\kappa=0.41$
λ	thermal conductivity of fluid, W/m K
λ_b	mean bulk thermal conductivity of SCO2 in the hot side of heat exchanger, W/m K
μ	dynamic viscosity of fluid, Pa.s
μ_b	bulk mean dynamic viscosity of fluid, Pa.s
μ_t	turbulent eddy viscosity, Pa.s
ν	kinematic viscosity of fluid, m^2/s
ξ_1, ξ_2	auxiliary variables in the F_1 expressions
ξ_3	auxiliary variable in the μ_t expression of the shear stress transport model
ρ	density of fluid, kg/m^3
ρ_b	mean bulk density of SCO2 in the hot side of heat exchanger, kg/m^3
σ_{k1}	model constant in the k-equation of the Wilcox k-ω model, $\sigma_{k1}=2$
σ_{k2}	model constant in the k-equation of the standard k-ε model, $\sigma_{k2}=1$
σ_{k3}	blended model constant in the k-equation of the blended Wilcox k-ω and standard k-ε models, $\sigma_{k3}=F_1\sigma_{k1}+\beta_1(1-F_1)\sigma_{k2}$
τ_w	wall shear stress, Pa
ϕ	porosity of heat exchanger
ψ	performance evaluation criterion for heat transfer enhancement
ω	rate of dissipation per unit turbulent kinetic energy, 1/s
ω_n	total ω near wall, 1/s
$\omega_{log}, \omega_{vis}$	ω values calculated by the solutions in the logarithmic and linear near-wall regions, 1/s

Subscript

i, j	index of the Cartesian coordinate system
x, y, z	Cartesian coordinate directions

Abbreviation

|	
2D	two-dimensional
3D	three-dimensional
CFD	computational fluid dynamics
CO2	carbon dioxide
CO2BOL	CO2 binding organic liquids
FEM	finite element method
PEC	performance evaluation criterion
PCHE	printed circuit heat exchanger
RANS	Reynolds-averaged Navier-Stokes equations
RGP	real gas property
SCO2	supercritical carbon dioxide
SST	shear stress transport
TPMS	triply periodic minimal surface

Schwarz-D structure was designed by using Mathematica in controllably cell size and fabricated with 3D printing technique. Compared with the shell-and-tube heat exchanger, the heat exchanger with TPMS Schwarz-D structure occupied 32 % less volume in the same heat transfer surface area and hydraulic diameter. The friction factor for the shell-and-tube heat exchanger was similar to the trends of the heat exchanger with the Schwarz-D geometrical structure [10]. A TPMS cross-flow heat exchanger was designed by utilizing the simple implicit functions for TPMS with parameters such as periodic length and offset parameter. The thermal and hydraulic performance of the heat exchanger was predicted in CFD code COMSOL and a parametric study on TPMS was carried out. It was shown that heat transfer rates were improved by a factor of 7.5 times in comparison to a traditional plate heat exchanger [11].

The thermal and hydraulic performance of counter-flow heat exchangers, which were composed of a core structure such as TPMS Schwarz-P, Schwarz-D and Schoen-G was predicted using the CFD software Star CCM + in laminar flow regime based on the 3D steady Navier-Stokes equations and energy equation. The fluid domain included one TPMS cell and the fluid velocity and temperature were given to cover Reynolds number in the range of 5–150. The reference heat exchanger is a two-dimensional (2D) flat plate counter-flow heat exchanger. The thermal and hydraulic performance of Schwarz-D seems to be best in heat transfer enhancement compared with Schwarz-P and Schoen-G in laminar flow regime [12].

Two counter-flow heat exchangers respectively with TPMS Schwarz-D and Schoen-G core structures were designed, and the corresponding manifolds were developed. Two complete heat exchangers were produced in the material AlSi10Mg, tested and simulated by using CFD software. The performance of the two exchangers was similar, but the heat exchanger with TPMS Schwarz-D was simpler and more symmetrical and was recommended [13].

The conjugate heat transfer in two heat exchangers with TPMS Schwarz-P, Schwarz-D and Schoen-G structures was analysed by using an in-house code of the 3D lattice Boltzmann method when the Reynolds
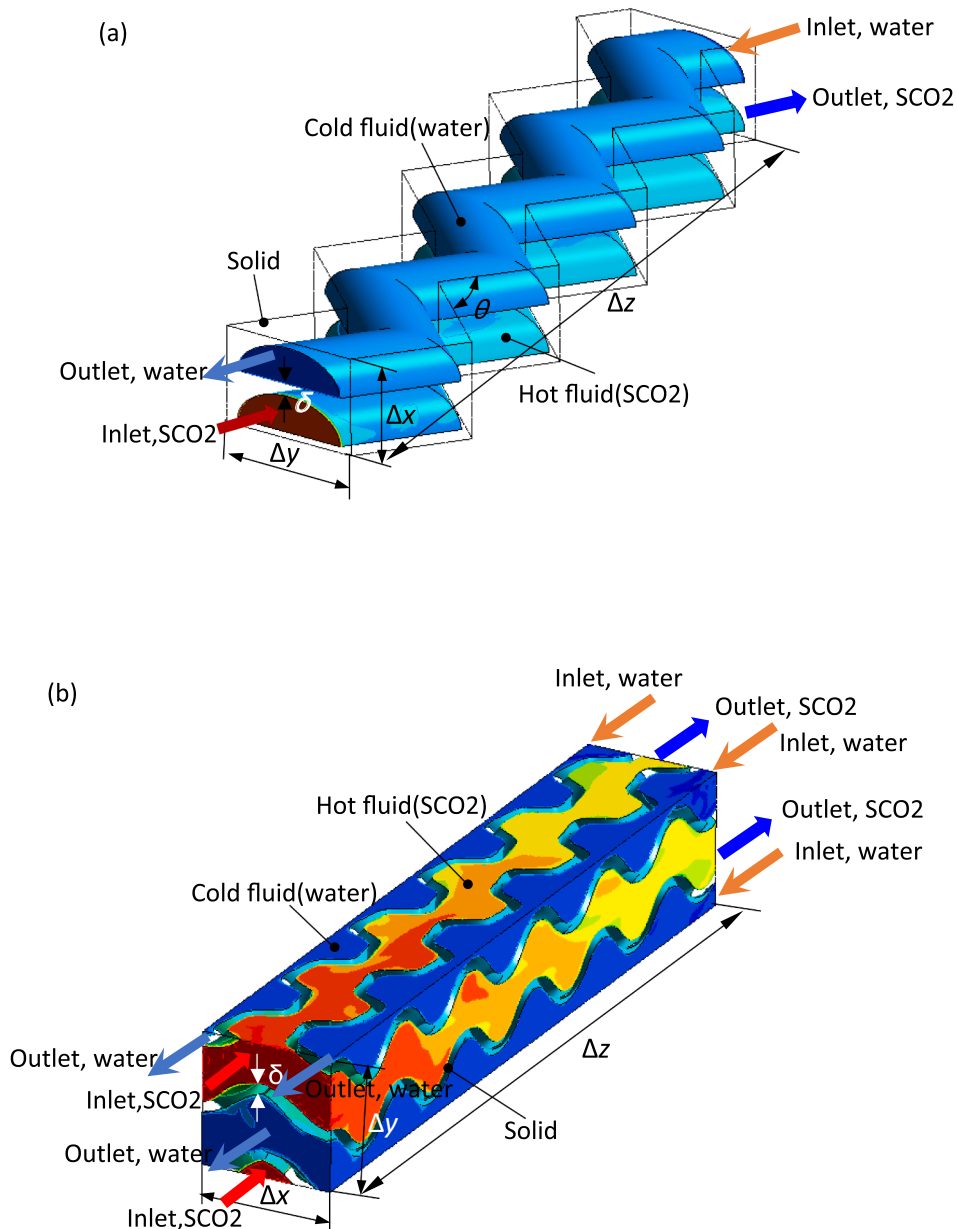
Fig. 1. Sketch of the TPMS Schoen-G heat exchanger and PCHE as well as their geometrical parameters, (a) PCHE, (b)TPMS Schoen-G heat exchanger, the coloured bodies are either SCO2 or water.

number is <2. The TPMS Schoen-G heat exchanger had the highest heat transfer rate than the Schwarz-P and Schwarz-D. However, the Schwarz-P structure had the lowest tortuosity and thus pressure drop amongst the exchangers [14].

The conjugate heat transfer in two counter-flow heat exchangers with TPMS Schwarz-D and Schoen-G structures was analysed by using CFD software-ANSYS CFX 15.0 based on the 3D steady Reynolds-averaged Navier-Stokes equations (RANS), energy equation and shear stress transport (SST) turbulence model. The reference heat exchanger is a printed circuit heat exchanger (PCHE). The supercritical carbon dioxide (SCO2) at different inlet temperatures and mass flow rates served as the cold and hot fluids, respectively. The Reynolds number was ranged in 2300–53,000 for the hot side, 3000–70,000 for the cold side. The performance evaluation criterion (PEC) ψ values of the heat exchangers with Schwarz-D and Schoen-G structures decreased with increasing Reynolds number Re, but the ψ values of the heat exchanger with Schoen-G varied little with Re, especially, ψ=1.75–1.10 in the hot side and ψ = 1.9–1.15 in the cold side for the Schwarz-D, ψ=1.35–1.18 in the hot side andψ = 1.3–1.4 in the cold side for the Schoen-G [15].

A volumetric distance field-based design method was developed for generating a compact heat exchanger with a TPMS core structure. The TPMS core structure, heat exchanger exterior shape, inlet and outlet are expressed by volumetric distance field variables. At most experimental flow rates, the 3D printed heat exchangers with TPMS core structure had much better heat transfer performance than the conventional plate heat exchanger due to the large heat transfer area density and continuous and fully interconnected flow paths in the TPMS core structure. However, the pressure drop across the TPMS compact heat exchangers was almost identical to the pressure drop in the conventional plate heat exchangers [16].

A microstructure TPMS heat exchanger with Schoen-G structure in $32.2 \times 32.2 \times 32.2$ mm volume was fabricated with 3D printing technique, and its thermal and hydraulic performance was tested at flow rates of 100–270 ml/min, the experimental heat transfer coefficient was ranged in 120–160 W/m^{2}K when the Reynolds number of hot fluid varied in 10–40 [17].

Water-cooled SCO2 counter-flow tube-in-tube heat exchangers may have an application in cooling or cold storage systems employing carbon dioxide (CO2) hydrate slurry as a working fluid and storage medium. The thermophysical properties of SCO2 change substantially with temperature and pressure, especially near the critical/pseudocritical point. Since SCO2 possesses a lower overall heat transfer coefficient than water, SCO2 convective heat transfer in a SCO2 heat exchanger needs to be enhanced to improve its effectiveness and reduce its size. However, heat transfer enhancement techniques in water-cooled SCO2 counter-flow tube-in-tube heat exchangers are very limited presently, for example, spiral fins in the tube wall, which could improve the heat transfer coefficient in the finned tubes by 1.4–2.0 [18] or 1.20–1.38 [19] times better than the smooth tube.

To achieve even high heat transfer enhancement, the other heat transfer enhancement methods should be sought out. Interestingly, TPMS structures, especially the Schoen-G, exhibited a good potential in applications to heat exchangers in SCO2 Brayton power cycles compared with a PCHE [15]. In that study, the TPMS and PCHE heat exchangers served as a counter-flow recuperator where both the hot fluid and cold

fluid were SCO2, and the inlet temperatures of both hot and cold SCO2 remained fixed, but the SCO2 flow rate was changed to obtain the expected SCO2 Reynolds numbers.

Clearly, whether TPMS heat exchangers can be applied to cooling or cold storage systems as a cooler of SCO2 when SCO2 is employed as a working medium is unexplored and unknown. In the present paper, the conjugated heat transfer in the TPMS Schoen-G heat exchanger and PCHE was predicted with CFD software ANSY CFX 19R2 at a fixed SCO2 flow rate but variable SCO2 inlet temperatures when the cold fluid is water at a fixed inlet temperature and flow rate. The thermal and hydraulic performance of the TPMS Schoen-G heat exchanger was assessed against that of the PCHE. The objective of the study is to check whether the TPMS Schoen-G heat exchanger and PCHE in Ref. [15] can be potentially applicable to cooling or cold storage systems using CO2 hydrate slurry as both working fluid and storage medium which was proposed by us in a granted project in terms of heat transfer enhancement point of view. This kind of investigation is not documented in the literature currently.

2. Computational models

2.1. The TPMS Schoen-G heat exchanger and PCHE

The PTMS Schoen-G heat exchanger and PCHE in Ref. [15], as shown in Fig. 1, were considered here, their geometrical parameters are listed in Table 1. Those heat exchangers are unit heat exchangers and repeated in the x-, y- and z-directions. It is assumed that conjugated heat transfer in every unit heat exchanger is approximately identical to that in the entire heat exchanger, thus the thermal and hydraulic performance of a unit heat exchanger can represent the performance of the entire exchanger. In each unit heat exchanger, there are the channels for the hot fluid-SCO2 and the channels for cold fluid-water. SCO2 flow and water flow in them in counter-direction. The two fluids are separated by a solid steel/metal sheet.

The hydraulic diameter d_h in Table 1 is determined with porosity ϕ and specific solid–fluid interface area ζ of hot or cold side of heat exchanger by using the following expression:

$$d_h = \frac{4\phi}{\zeta} \tag{1}$$

where the porosity ϕ is defined as the fraction of the volume of voids over the total volume in heat exchanger, ϕ=1 for PCHE, ϕ<1 for TPMS heat exchanger; the specific solid–fluid interface area ζ is the solid–fluid interface area per unit volume.

2.2. Fluid flow and heat transfer models

The CFD software ANSYS CFX 2019R2 was adopted to carry out conjugated heat transfer simulations of SCO2 and water here. The SCO2 is considered a compressible gas, its thermophysical properties depend on both temperature and pressure. The cold water is an incompressible liquid. The flow of SCO2 or cold water is 3D, steady and turbulent. The RANS equations and energy equation for the flows of SCO2 or water are written as [20].

$$\frac{\partial}{\partial x_j}\left(\rho u_j\right) = 0 \tag{2}$$

$$\frac{\partial}{\partial x_j}\left(\rho u_i u_j\right) = -\frac{\partial}{\partial x_i}\left(p + \frac{2}{3}\rho k\right) + \frac{\partial}{\partial x_j}\left[(\mu + \mu_t)\left(\frac{\partial u_i}{\partial x_j} + \frac{\partial u_j}{\partial x_i}\right)\right] + \rho g_i \tag{3}$$

$$\frac{\partial}{\partial x_j}\left[\rho u_j\left(h + \frac{1}{2}u_i u_i + k\right)\right] = \frac{\partial}{\partial x_j}\left(\lambda\frac{\partial T}{\partial x_j} + \frac{\mu_t}{Pr_t}\frac{\partial h}{\partial x_j}\right) + S_E \tag{4}$$

where ρ is the density of SCO2 or water, u_i and u_j are the Reynolds or time-averaged velocity of SCO2 in the coordinate x_i and x_j directions,

Table 1
Geometrical parameters of TPMS Schoen-G heat exchanger and PCHE.

Parameter	PCHE	Schoen-G
Δx(mm)	4.89	3.77
Δy(mm)	3.25	3.77
Δz(mm)	24	24
d_h(mm)	1.62	1.61
δ(mm)	0.7	0.7
θ(°)	90	N/A

Table 2

Flow and thermal conditions used in conjugated heat transfer simulations of TPMS Schoen-G heat exchanger and PCHE.

Fluid	Parameter	PCHE	Schoen-G
SCO2	p_1(MPa)	8, 9	8, 9
	T_1(℃)	65–30	65–30
	G(kg/m^{2}s)	250	400
Cold water	T_1(℃)	25	25
	m_f(m^3/s)	5×10^{-6}	5×10^{-6}

respectively; i and j are the coordinate index, i, j=1,2,3; p is the pressure of SCO2 or water, k is the turbulent kinetic energy, $k = \frac{1}{2}\overline{u_i'^2}$, u_i' is turbulent fluctuation velocity of SCO2, μ is the dynamic viscosity of SCO2 or water,; μ_t is the turbulent eddy viscosity, g_i is the unit body force,$g_i = 0$ is held here, h is the enthalpy of SCO2, λ is the thermal conductivity of SCO2 or water, T is the temperature of SCO2 or water, Pr_t is the turbulent Prandtl number, Pr_t=0.9, S_E is the source term of energy, S_E=0 here; ρ, μ and λ are given by the RGP table for SCO2.

The SST turbulence model was employed. The model is a blend of the Wilcox k-ω model and the standard k-ε model, where the flow with a low Reynolds number near the wall is treated by the k-ω model, while the core flow with a high Reynolds number is handled by the standard k-ε model. Further, the SST is considered to suppress an overpredicted turbulent eddy viscosity [21]. The Wilcox k-ω model reads as [20].

$$\frac{\partial}{\partial x_j}\left(\rho u_j k\right) = \frac{\partial}{\partial x_j}\left[\left(\mu + \frac{\mu_t}{\sigma_{k1}}\right)\frac{\partial k}{\partial x_j}\right] + P_k - \beta_k \rho k\omega + P_{kb} \tag{5}$$

$$\frac{\partial}{\partial x_j}\left(\rho u_j \omega\right) = \frac{\partial}{\partial x_j}\left[\left(\mu + \frac{\mu_t}{\sigma_{\omega1}}\right)\frac{\partial \omega}{\partial x_j}\right] + \frac{\alpha_1}{\nu_t}P_k - \beta_1 \rho k\omega^2 + P_{\omega b} \tag{6}$$

where σ_{k1}, β_k, $\sigma_{\omega1}$, α_1 and β_1 are the model constants, σ_{k1}=$\sigma_{\omega1}$ = 2, α_1=5/9, β_k=0.09, β_1=0.075, P_k is the turbulence production term, $P_k = \mu_t\left(\frac{\partial u_i}{\partial x_j}+\frac{\partial u_j}{\partial x_i}\right)\frac{\partial u_i}{\partial x_j}-\frac{2}{3}\frac{\partial u_k}{\partial x_k}\left(3\mu_t\frac{\partial u_k}{\partial x_k}+\rho k\right)$, P_{kb} and $P_{\omega b}$ are the buoyancy production term in the k-equation and ω-equation,and ignored due to low SCO2 inlet temperature. The transformed standard k-ε model is given by:

$$\frac{\partial}{\partial x_j}\left(\rho u_j k\right) = \frac{\partial}{\partial x_j}\left[\left(\mu + \frac{\mu_t}{\sigma_{k2}}\right)\frac{\partial k}{\partial x_j}\right] + P_k - \beta_k \rho k\omega + P_{kb} \tag{7}$$

$$\frac{\partial}{\partial x_j}\left(\rho u_j \omega\right) = \frac{\partial}{\partial x_j}\left[\left(\mu + \frac{\mu_t}{\sigma_{\omega2}}\right)\frac{\partial \omega}{\partial x_j}\right] + \frac{\alpha_2}{\nu_t}P_k - \beta_2 \rho k\omega^2 + \frac{2\rho}{\sigma_{\omega2}\omega}\frac{\partial k}{\partial x_j}\frac{\partial \omega}{\partial x_j} + P_{\omega b} \tag{8}$$

where σ_{k2}, $\sigma_{\omega2}$, α_2 and β_2 are the model constants, σ_{k2}=1, $\sigma_{\omega2}$=1/0.856, α_2=0.44, β_2=0.0828. Eqs. (5) and (7), Eqs. (6) and (8) are blended as$F_1 \times$ Eq. (5)+(1-F_1) $\times$ Eq. (7) and$F_1 \times$ Eq. (6)+(1-F_1) $\times$ Eq. (8) with a bending function F_1, whereF_1 = 1 at the wall, F_1=0 in the core flow, and $0<F_1 < 1$ between the wall and the core flow, leading to the following blended k-ω model [20,21]:

$$\frac{\partial}{\partial x_j}(\rho u_j k) = \frac{\partial}{\partial x_j}[(\mu + \frac{\mu_t}{\sigma_{k3}})\frac{\partial k}{\partial x_j}] + P_k - \beta_k \rho k\omega + P_{kb} \tag{9}$$

$$\frac{\partial}{\partial x_j}(\rho u_j \omega) = \frac{\partial}{\partial x_j}\left[\left(\mu + \frac{\mu_t}{\sigma_{\omega3}}\right)\frac{\partial \omega}{\partial x_j}\right] + \frac{\alpha_3}{\nu_t}P_k - \beta_3 \rho k\omega^2 + (1-F_1)\frac{2\rho}{\sigma_{\omega2}\omega}\frac{\partial k}{\partial x_j}\frac{\partial \omega}{\partial x_j} + P_{\omega b} \tag{10}$$

$$F_1 = \tanh(\xi_1^4), \xi_1 = \min\left(\max\left(\frac{\sqrt{k}}{\beta_k\omega y_n}, \frac{500\nu}{y_n^2\omega}\right), \frac{4\rho k}{\xi_2 \sigma_{\omega2}y_n^2}\right), \xi_2$$
$$= \max\left(\frac{2\rho}{\sigma_{\omega2}\omega}\frac{\partial k}{\partial x_j}\frac{\partial \omega}{\partial x_j}, 1.0 \times 10^{-10}\right) \tag{11}$$

where σ_{k3}, $\sigma_{\omega3}$, α_3 and β_3 are the constants blended, $\sigma_{k3} = F_1\sigma_{k1} + \beta_1(1 -$

$F_1)\sigma_{k2}$, $\sigma_{\omega3} = F_1\sigma_{\omega1} + (1 - F_1)\sigma_{\omega2}$, $\alpha_3 = F_1\alpha_1 + (1 - F_1)\alpha_2$,
and $\beta_3 = F_1\beta_1 + (1 - F_1)\beta_2$, ν is the kinematic viscosity of SCO2 or water, y_n is the distance the nearest wall. The SST is realised by suppressing overpredicted eddy viscosity as [21]:

$$\mu_t = \min\left(\frac{\rho k}{\omega}, \frac{a_1\rho k}{\gamma F_2}\right), \gamma = \sqrt{2\gamma_{ij}\gamma_{ij}}, \gamma_{ij} = \frac{1}{2}\left(\frac{\partial u_i}{\partial x_j}+\frac{\partial u_j}{\partial x_i}\right), F_2 = \tanh(\xi_2^2), \xi_2$$
$$= \max\left(\frac{2\sqrt{k}}{\beta_k\omega y_n}, \frac{500\nu}{y_n^2\omega}\right) \tag{12}$$

where a_1 is a constant,$a_1 = 0.31$, γ_{ij} represent strain rate tensor, γ is magnitude of strain rate.

The low-Reynolds number model for the viscous sublayer is replaced with a blended wall function, i.e., Automatic Near-Wall Treatment in the SST model. The blended wall function is related to $y^+(=u_\tau y_n/\nu)$, where u_τ is the friction velocity of the fluid at the wall, determined by $\tau_w = \rho u_\tau^2$, τ_w is wall shear stress. Based on both ω and u_τ, the blended wall function is expressed by Ref. [21]:

$$\begin{cases} \omega_n = \sqrt{\omega_{vis}^2 + \omega_{log}^2}, \omega_{vis} = \frac{6\nu}{\beta_1 y_n^2}, \omega_{log} = \frac{u_\tau}{a_1\kappa y_n} \\ u_\tau = \sqrt[4]{\left(u_\tau^{vis}\right)^4 + \left(u_\tau^{log}\right)^4}, u_\tau^{vis} = \frac{u_n}{y^+}, u_\tau^{log} = \frac{u_n}{\frac{1}{\kappa}\ln(y^+) + B} \end{cases} \tag{13}$$

where ω_{vis} and ω_{log} are ω values given by the solutions in the linear and the logarithmic near-wall regions, ω_n is the total ω near wall, u_τ^{vis} and u_τ^{log} are the friction velocities calculated by using the linear and logarithmic solutions in the sublayer layer, u_n is fluid velocity near wall, B is constant, B=5.2 for hydraulically smooth walls. The fluxes in the momentum equations and the k equation at wall are referred to Ref. [20].

To determine the dimensionless temperature profile across the sublayer, the following empirical expression proposed by Ref. [22] is employed in ANSYS CFX [21 22]:

$$\begin{cases} T^+ = Pry^+ e^{-\Gamma} + [0.1\ln(y^+) + \beta]e^{-1/\Gamma}, \Gamma = \frac{0.01(Pry^+)^4}{1 + 5Pr^3 y^+} \\ q_w = \frac{\rho C_p u_\tau}{T^+}(T_w - T_n), Pr = \frac{\mu C_p}{\lambda}, \beta = \left(3.85Pr^{1/3} - 1.3\right) + 0.1\ln(Pr) \end{cases} \tag{14}$$

where Γ is auxiliary variable of both Pr and y^+, q_w is wall heat flux, C_p is specific heat capacity of fluid, T^+ is dimensionless temperature in boundary layer, T_w is wall temperature, T_n is fluid temperature in the first mesh layer, β is auxiliary variable of Pr, Pr is Prandtl number of fluid. According to Eqs. (13) and (14), the shear stress, wall temperature or heat flux can be calculated.

A real gas property (RGP) table was generated for SCO2 by using the REFPROP version 9.0 program issued by the National Institute of Standards and Technology and then read into CFX, the SCO2 thermophysical property constants are interpolated with local temperature and pressure in conjugated heat transfer simulations. The thermophysical property constants of cold water remain unchanged with temperature and pressure in the simulations.

The flow and thermal conditions for conjugated heat transfer simulations of TPMS Schoen-G heat exchanger and PCHE are listed in Table 2. The inlet temperature and mass flow rate of the cold water remain unchanged for two heat exchangers. The simulations took place at different inlet temperatures and pressures of SCO2 to clarify their effects on the thermal and hydraulic performance of those heat exchangers when the inlet temperature and mass flow rate of the cold water remained unchanged.

In the Solver Control of CFX, the high-resolution scheme was chosen for the advection terms in the Navier-Stokes equations and energy equation, but the first order scheme was specified for the advection
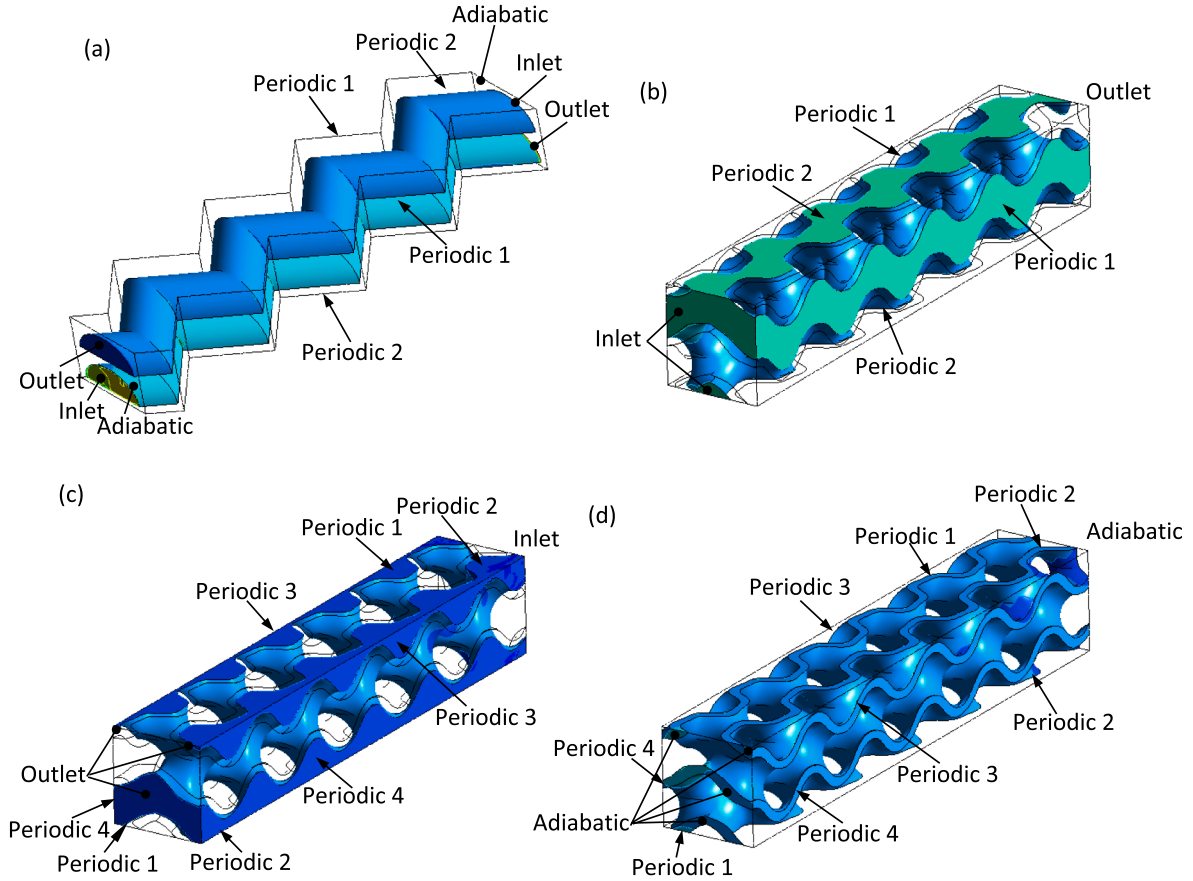
Fig. 2. Sketch of boundary conditions in the fluid domains of PCHE and TPMS heat exchanger, (a) PCHE, (b) hot fluid, (c) cold fluid and (d) metal sheet for the TPMS heat exchanger, Periodic 1, Periodic 2,.., Periodic 4 represent a pair of surfaces for translational periodicity condition.

terms in the SST model. The second order scheme was used to the diffusion terms in the models.

2.3. Boundary conditions

The boundary conditions are shown schematically in Fig. 2. There are three computational domains, i.e., hot SCO2, cold water and solid metal sheet. Each domain has an inlet and outlet. Mass flow rate, flow direction, 5 % turbulence intensity and temperature are specified in the inlet of the hot SCO2 domain, and pressure is given in the outlet of the hot SCO2. Zero pressure, temperature, zero gradient of flow variables and temperature are imposed in the inlet of the cold water domain, and mass flow rate with uniform mass flux constraint is implemented in the outlet of the domain. The inlet and outlet of the solid metal sheet domain are adiabatic.

Two solid–fluid domain interfaces are established on the boundaries of the hot SCO2 domain and the solid metal sheet domain, and on the boundaries of the cold water domain and the solid metal sheet domain. The translational periodicity condition is generated on each pair of the opposite external surfaces of each domain.

Note that the pressure in the inlet but the mass flow rate in the outlet of the hot SCO2 domain was imposed in Ref. [23]. Initially, that boundary setup was adopted, unfortunately, this setup resulted in an imbalance of mass flow rate between the inlet and the outlet in TPMS Schoen-G heat exchanger with multiple channels in the inlet and outlet. Therefore, the mass flow rate in the inlet but the pressure in the outlet of the hot SCO2 domain was specified to achieve an exact balance in mass flow rate of SCO2 here.

2.4. Mesh size independence

Mesh size independence exercises were carried out on the two heat exchangers at the inlet temperature $T_1 = 65℃$ and inlet pressure $p_1 = 8$ MPa of SCO2. Four sets of mesh in the TPMS Schoen-G heat exchanger and two sets of mesh in PCHE were generated and illustrated in Fig. 3 (a) and (b), and the information on the meshes is tabulated in Table 3. In those meshes, tetrahedral elements are dominant. To meet the $y^+{\approx}1$ condition required by the SST model [23], inflation boundary layer meshes near solid walls were generated. Since the velocity of water in the cold side was lower, the first layer height of 1×10^{-2}mm for TPMS Schoen-G heat exchanger or 2.5×10^{-3}mm for PCHE could yield the $y^+{\ll}1$ condition. For SCO2, however, the first layer height of 5×10^{-4}mm for TPMS Schoen-G heat exchanger and PCHE led to the $y^+{\approx}1$ condition as shown in Table 3.

The y^+, τ_w, Nu and f of SCO2 in TPMS Schoen-G heat exchanger are plotted as a function of number of elements in Fig. 3 (c) and (d). The mesh size independence is achieved between Mesh3 and Mesh4, hence Mesh4 is adopted in the conjugated heat transfer simulations in TPMS Schoen-G heat exchanger. The $y^+{\langle}1$ condition was guaranteed at Mesh6, therefore, Mesh6 was employed in the conjugated heat transfer simulations in PCHE.

2.5. Data reduction

The thermal and hydraulic performance of TPMS Schoen-G heat exchanger and PCHE is described by Nusselt number Nu and Darcy–Weisbach friction factor f. They are calculated by using the following expressions:
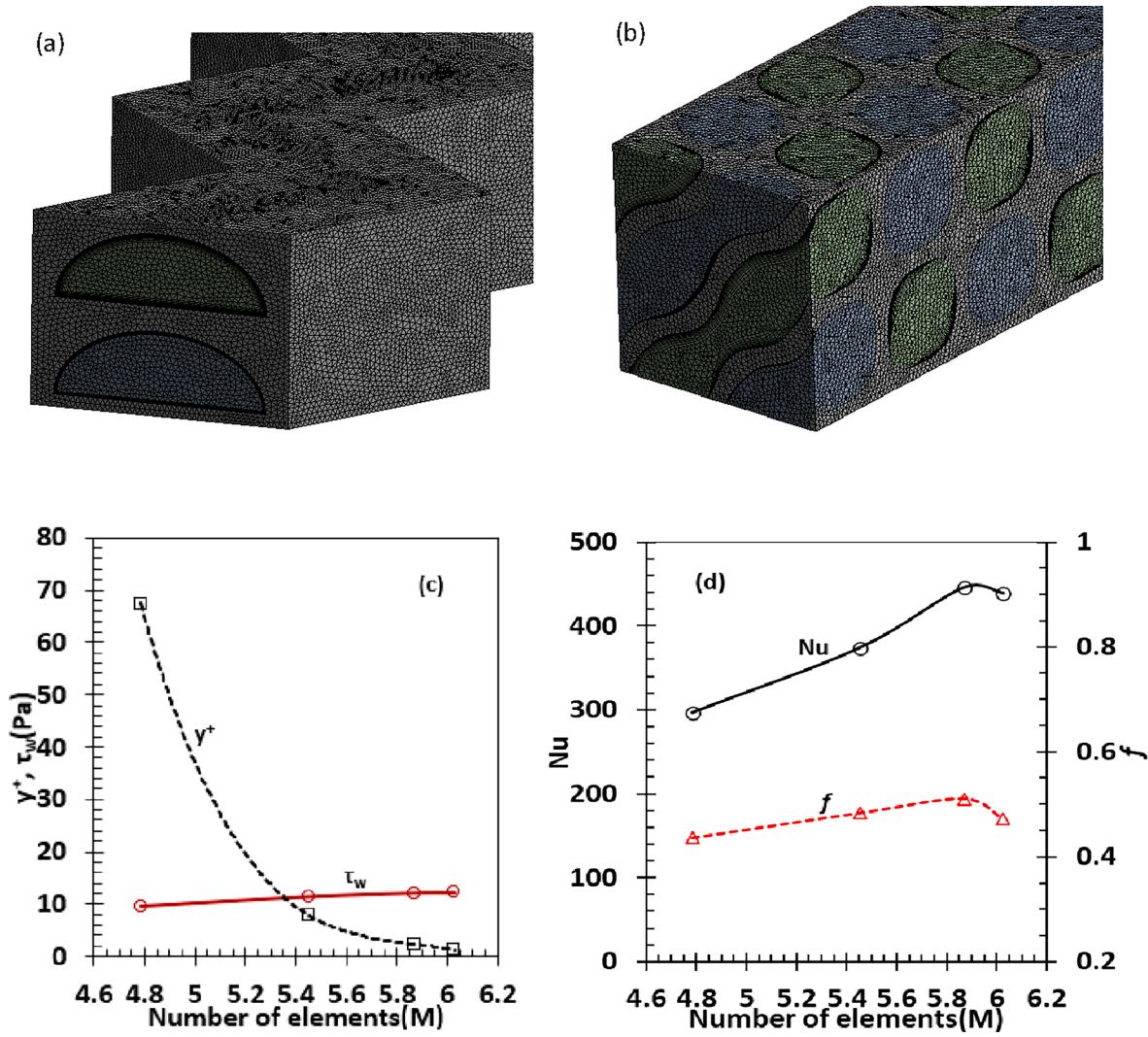
Fig. 3. Close-up views of TPMS Schoen-G heat exchanger and PCHE, (a)PCHE, (b)TPMS Schoen-G heat exchanger, (c) y^+ and τ_w versus number of elements curves for TPMS Schoen-G heat exchanger, (d) Nu and f versus number of elements curves for TPMS Schoen-G heat exchanger, M−million.

Table 3
Information on the meshes employed in CFD simulations of SCO2 in TPMS Schoen-G heat exchanger and PCHE.

Geometrical model		TPMS Schoen-G				PCHE	
Mesh name		Mesh1	Mesh2	Mesh3	Mesh4	Mesh5	Mesh6
Element size(mm)		0.45	0.4	0.4	0.4	0.4	0.4
Nodes		1,024,893	1,863,404	1,959,578	1,991,047	1,123,638	1,307,005
Elements	Total	3,209,717	5,452,188	3,963,019	6,025,853	3,704,734	3,963,019
	Tet4	2,181,136	3,199,831	3,551,895	3,698,200	2,447,182	2,286,283
		(68.0 %)	(58.7 %)	(60.5 %)	(61.4 %)	(66.1 %)	(58 %)
	Wed6	1,020,309	2,239,860	2,308,489	2,319,934	1,257,552	1,677,636
		(31.8 %)	(41.1 %)	(39.4 %)	(38.5 %)	(33.9 %)	(42 %)
	Pyr5	8,272(0.2 %)	12,497(0.2 %)	8,635(0.1 %)	7,719(0.1 %)	N/A	N/A
Element quality		0.7269 ± 0.2113	0.6393 ± 0.2755	0.6066 ± 0.3213	0.5958 ± 0.3378	0.5735 ± 0.3781	0.5308 ± 0.3705
Aspect ratio		2.97 ± 3.88	4.49 ± 5.78	10.09 ± 20.38	17.73 ± 40.61	17.51 ± 27.78	10.49 ± 40.28
Skewness		0.2792 ± 0.1542	0.2544 ± 0.1453	0.2408 ± 0.1352	0.2380 ± 0.1331	0.2073 ± 0.1281	0.2072 ± 0.1329
Orthogonal quality		0.7197 ± 0.1532	0.7447 ± 0.1444	0.7576 ± 0.1355	0.7593 ± 0.1394	0.7896 ± 0.1299	0.7899 ± 0.1358
Inflation mesh for boundary layer	First layer height (mm)	0.01	0.0035	0.001	0.0005	0.001	0.0005
	Number of layers	8	12	12	12	12	18
	Growth rate	1.2	1.2	1.2	1.2	1.2	1.2
	$T_1 = 65°C$ $p_1 = 8$ MPa	67.36	7.83	2.40	1.18	1.90	0.87

Tet4-four-node tetrahedron element, We6-six-node wedge element, Pyr5-five-node pyramid element, $y^+=\sqrt{\tau_w/\rho}y_n/\nu$, where τ_w is the shear stress at the wall, y_n is the distance to the nearest wall from the first mesh layer and ν is the local kinematic viscosity of SCO2.
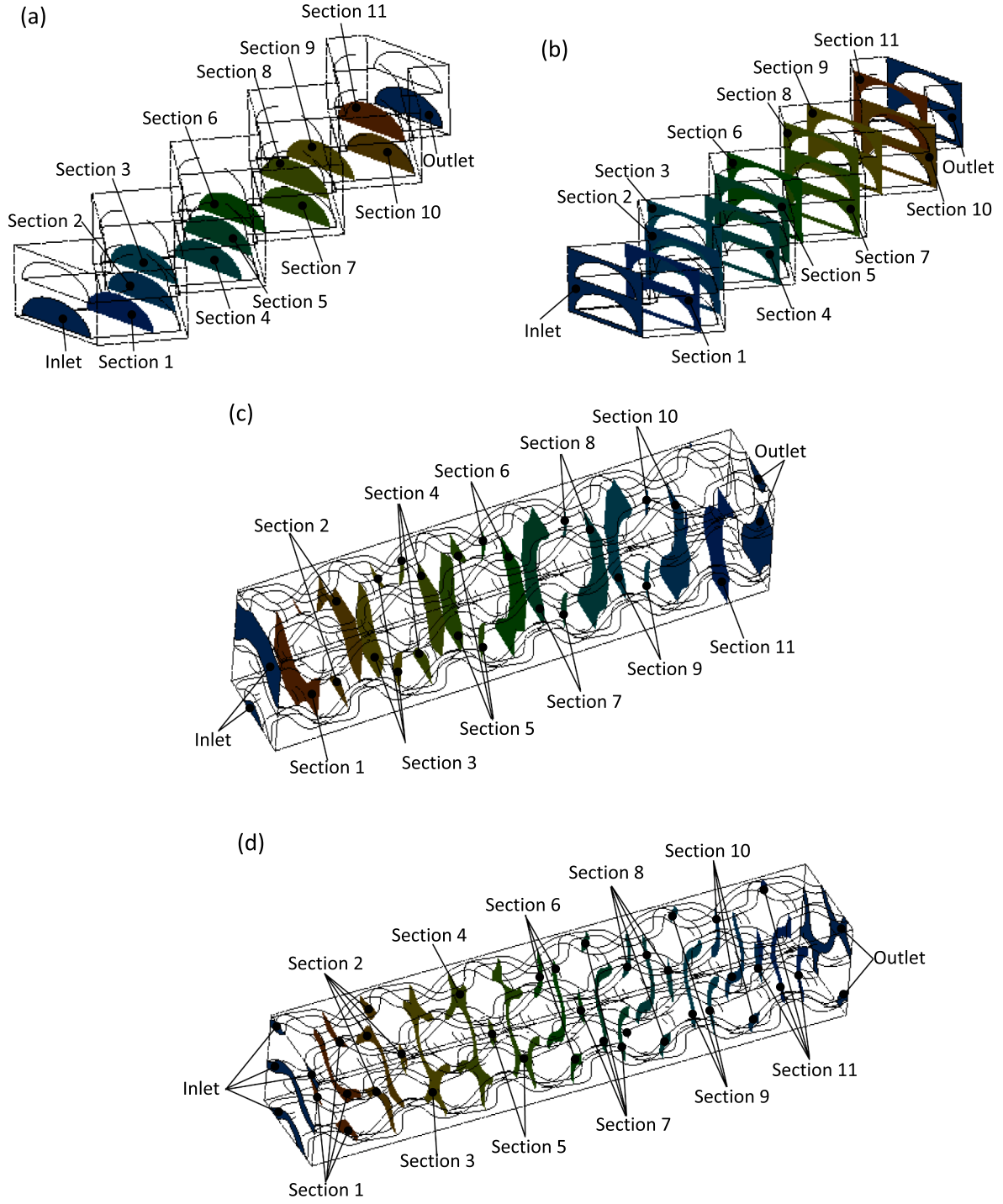
Fig. 4. Cross-sections (Section1, Section2,.., Section 11) created in the hot side and solid sheet of TPMS Schoen-G heat exchanger and PCHE, (a) cross-sections in the hot side of PCHE, (b) cross-sections in the solid sheet of PCHE, (c) cross-sections in the hot side of TPMS Schoen-G heat exchanger, (d) cross-sections in the solid sheet of TPMS Schoen-G heat exchanger, the shadows represent the cross-sections specified.

$$\begin{cases} f = \dfrac{\Delta p}{\rho_b \left(\dfrac{L_z}{d_h} \right) \left(\dfrac{1}{2} u_b^2 \right)} \\ Nu = \dfrac{U d_h}{\lambda_b}, U = \dfrac{q_w}{T_b - T_w} \end{cases} \quad (15)$$

where Δp is the pressure drop of SCO2 across the heat exchanger, ρ_b and u_b are the mean bulk density and bulk velocity of SCO2 in the hot side of the heat exchanger, U is the mean heat transfer coefficient between the SCO2 and the metal sheet wall, T_b and T_w are the mean bulk temperature of SCO2 in the hot side and the mean wall temperature, λ_b is the mean bulk thermal conductivity of SCO2 in the hot side. The parameters ρ_b, u_b, T_b, and λ_b were extracted in CFX-Post from the CFX result files by employing 11 cross-sections (Section 1, Section 2,.., Section 11) in the hot side of the heat exchanger with 2 mm apart but T_w by those in the solid metal sheet as shown in Fig. 4. First, those parameters were averaged in the 11 cross-sections plus the inlet and outlet. Then, the arithmetic mean of 13 averaged values was taken to obtain each mean bulk parameter.
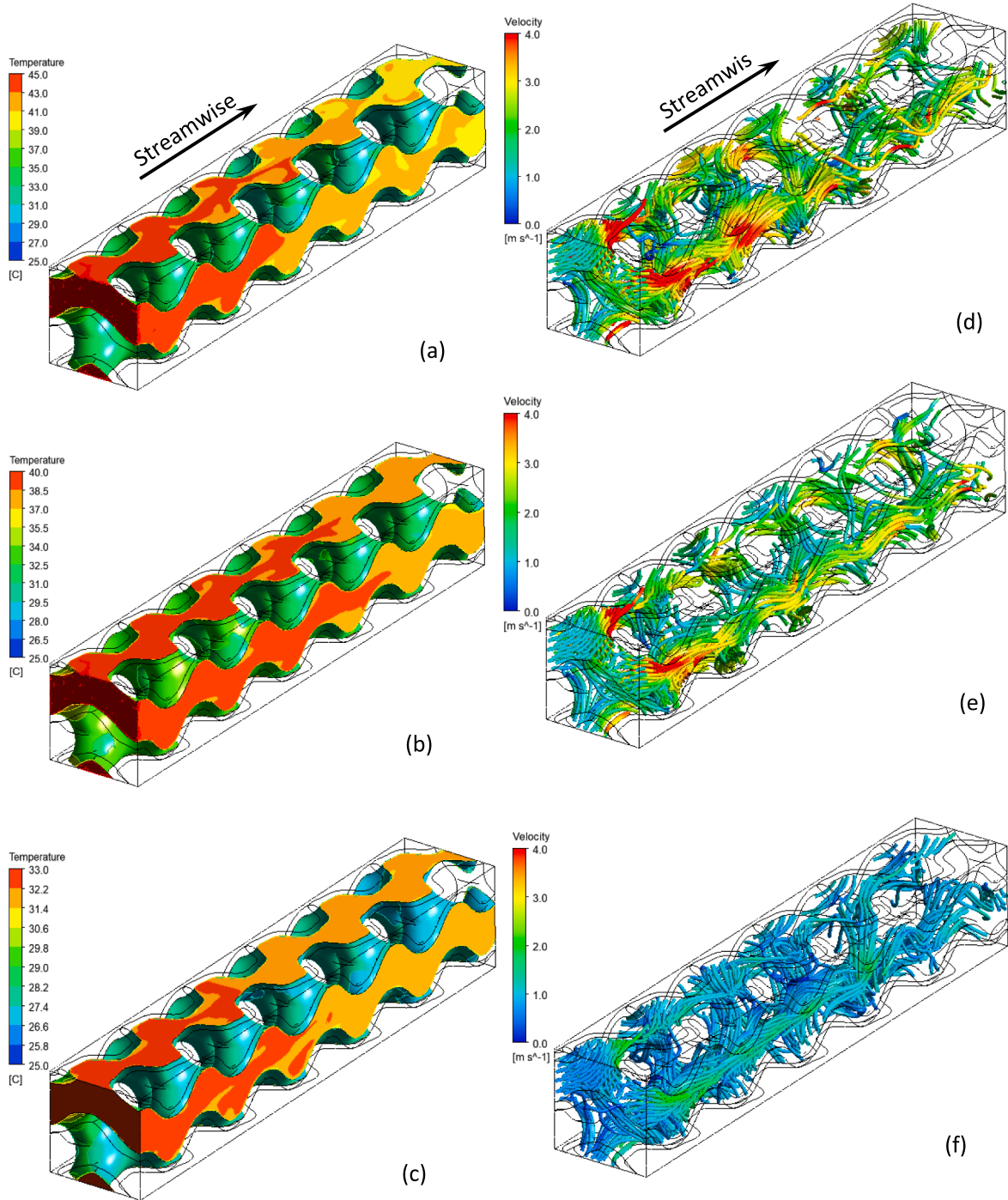
Fig. 5. Temperature contour and streamline of the hot side in TPMS Schoen-G heat exchanger at $T_1 = 45$, 40, 32.5℃ and $p_1 = 8$ MPa, (a)-(c) counter, (d)-(f) streamline, (a) & (d) for $T_1 = 45$℃, (b) & (e) for $T_1 = 40$℃, (c) & (f) for $T_1 = 32.5$℃.

The heat transfer enhancement of TPMS Schoen-G heat exchanger against PCHE is assessed by PEC ψ. PEC is defined as:

$$\psi = \frac{Nu/Nu_0}{\sqrt[3]{f/f_0}} \tag{16}$$

where f and Nu are the friction factor and Nusselt number of the TPMS Schoen-G heat exchanger, f_0 and Nu_0 are the friction factor and Nusselt number of the reference heat exchanger, i.e., PCHE.

3. Results

3.1. Flow and thermal details

The SCO2 temperature contour and streamline in the hot side of TPMS Schoen-G heat exchanger and PCHE at $p_1 = 8$ MPa, T_1=45, 40, 32.5℃ are illustrated in Fig. 5 and Fig. 6, respectively. The temperature of SCO2 body decreases downstream, especially for TPMS Schoen-G heat exchanger at a higher inlet temperature.
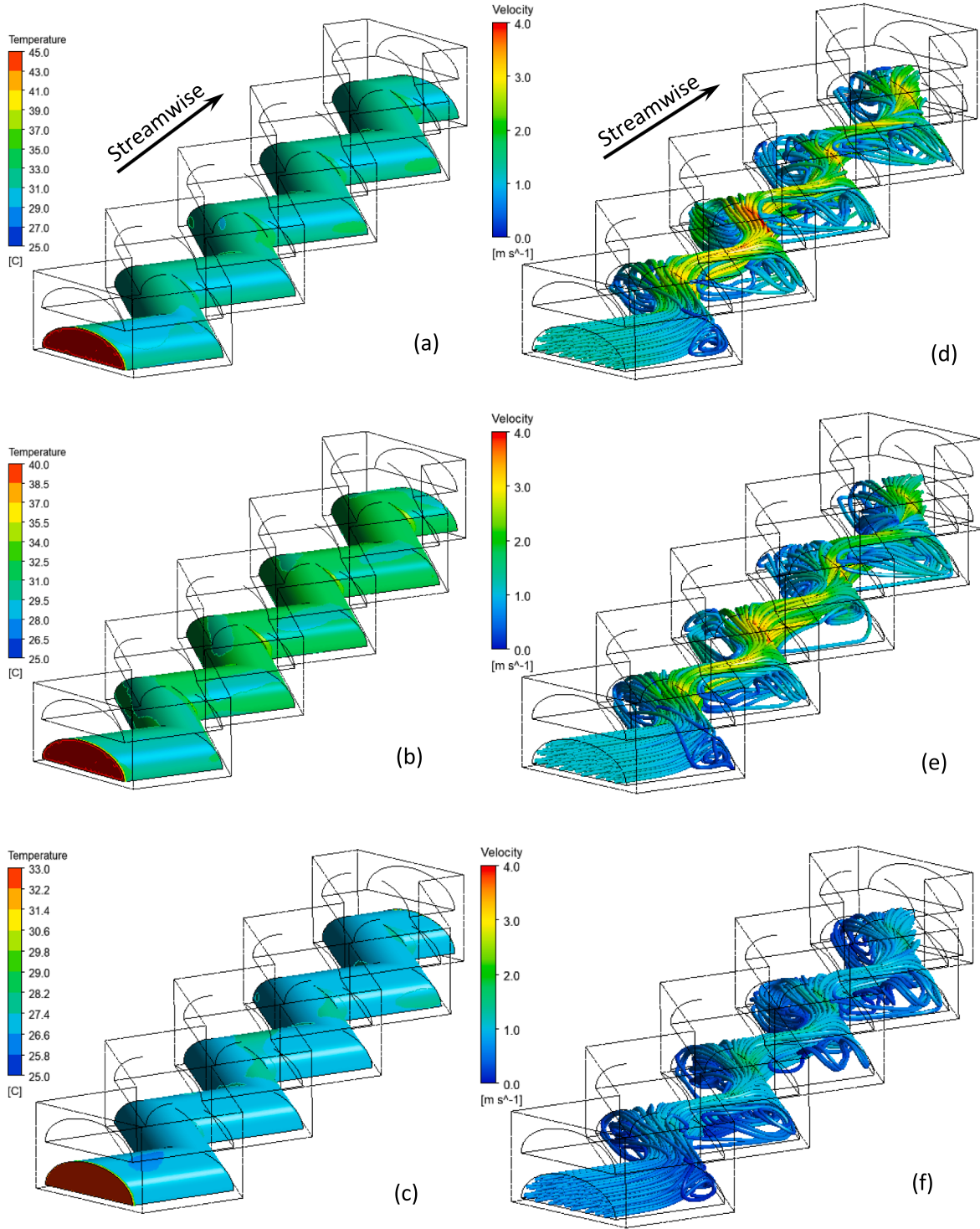
Fig. 6. Temperature contour and streamline of the hot side in PCHE at $T_1 = 45, 40, 32.5℃, p_1 = 8$ MPa, (a)-(c) contour, (d)-(f) streamline, (a) & (d) for $T_1 = 45℃$, (b) & (e) for $T_1 = 40℃$, (c) & (f) for $T_1 = 32.5℃$.

Although the flow channels are multi-connection in TPMS Schoen-G heat exchanger, the streamlines are very smooth downstream. A higher velocity occurs in the regions with greater curvature. With decreasing inlet temperature, the velocity distribution among streamlines becomes uniform apparently. The flow channels are single connection in PCHE, however, some streamlines near the wall are trapped in each corner of the channel, forming spiral flow patterns there. In fact, these spiral flow patterns are vortex regions and result in a significant hydraulic loss but

heat transfer enhancement. These vortex regions are responsible for the increased friction factor shown in Fig. 9 (a). Inlet temperature influences a little on the spiral flow patterns.

The cross-sectional averaged temperature T_s streamwise profile of SCO2, metal sheet and cold-water in the two heat exchangers at $p_1 = 8$ MPa, T_1=45, 40, 32.5℃ are illustrated in Fig. 7. The temperature difference ΔT_s profile between SCO2 and metal sheet is calculated and shown as well. At three inlet temperatures, the cross-sectional averaged
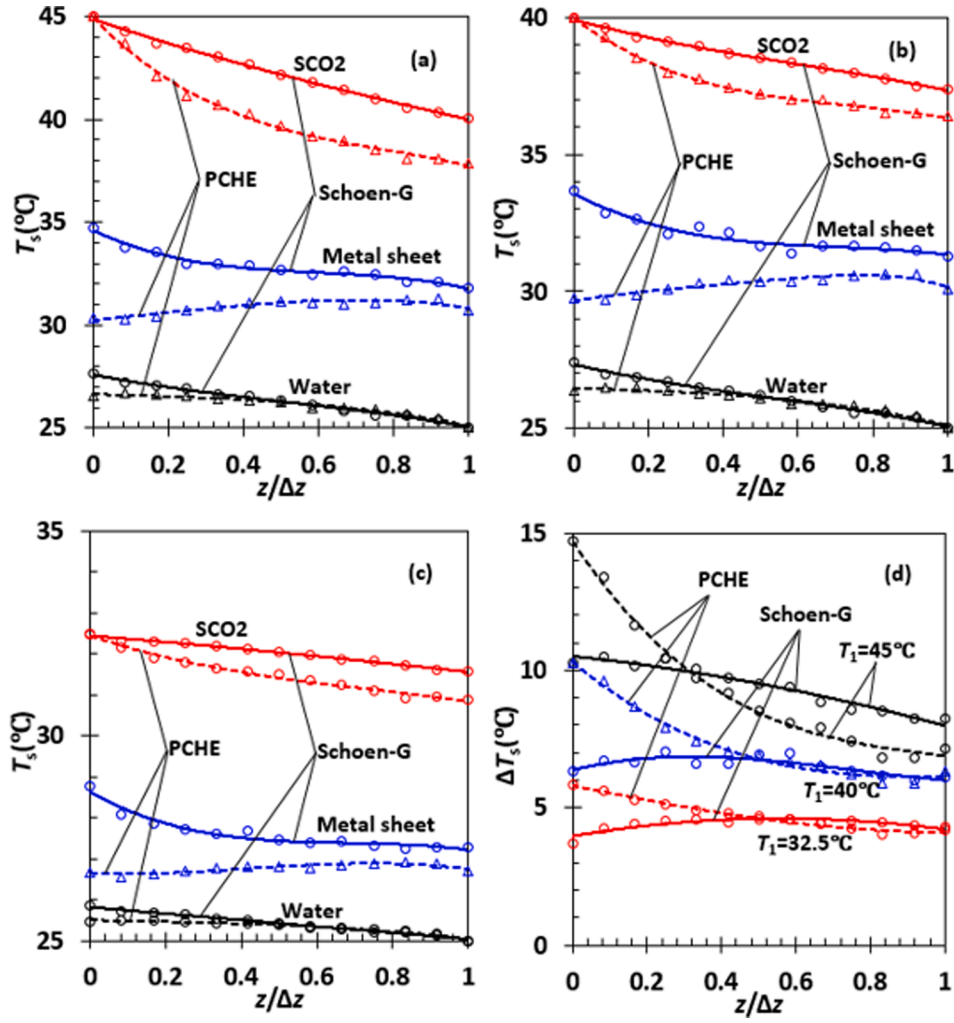
Fig. 7. Cross-sectional averaged temperature streamwise profile and temperature difference of SCO2, metal sheet and cold-water in TPMS Schoen-G heat exchanger and PCHE at $p_1 = 8$ MPa, (a) $T_1 = 45℃$, (b) $T_1 = 40℃$, (c) $T_1 = 32.5℃$.
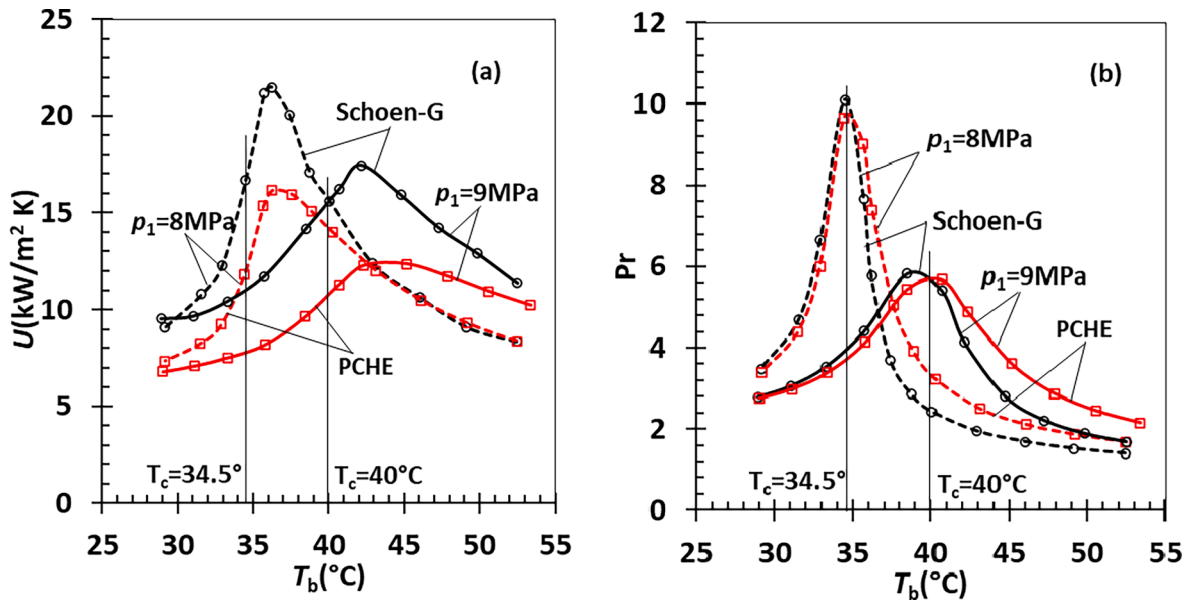
Fig. 8. Mean heat transfer coefficient U and Prandtl number Pr curves of SCO2 in the hot side in TPMS Schoen-G heat exchanger and PCHE in $p_1 = 8$, 9 MPa, (a) U curve, (b) Pr curve, $T_c = 34.5℃$ for $p_1 = 8$ MPa, $T_c = 40℃$ for $p_1 = 9$ MPa.
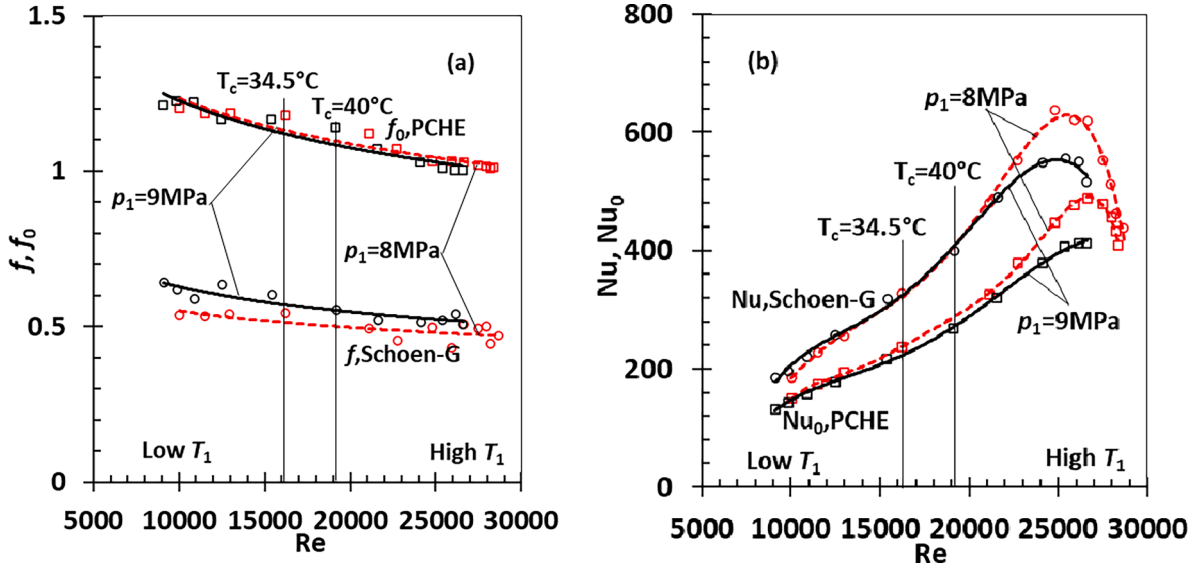
Fig. 9. Friction factors f and f_0, Nusselt numbers Nu and Nu_0 of TPMS Schoen-G heat exchanger and PCHE are plotted as a function of Reynolds number Re, (a) f and f_0, (b)Nu and Nu_0, $T_c = 34.5$℃ for $p_1 = 8$ MPa, $T_c = 40$℃ for $p_1 = 9$ MPa.

Fig. 10. Friction factor ratio f/f_0, Nusselt number ratio Nu/Nu_0 and PEC ψ of TPMS Schoen-G heat exchanger against PCHE at $T_1 = 32.5$℃ for $p_1 = 8$ MPa, $T_1 = 40$℃ for $p_1 = 9$ MPa (a), and the mean Prandtl number Pr and dynamic viscosity of TPMS Schoen-G heat exchanger (b).

temperature T_s of SCO2 declines streamwise gradually, while the temperature of cold water rises streamwise step-by-step. The temperature profile of SCO2 in PCHE goes down steeper toward the outlet than TPMS Schoen-G heat exchanger. However, the temperature pro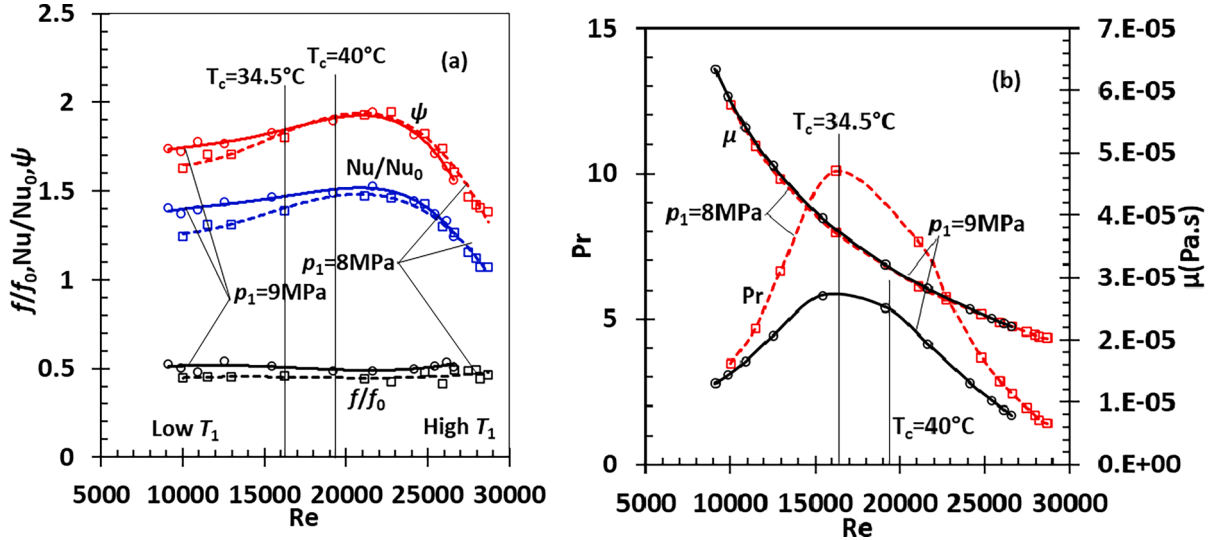file of cold water in PCHE climbs faster than TPMS Schoen-G heat exchanger. The cross-sectional averaged temperature is in-between SCO2 and cold water. The temperature of the metal sheet in TPMS Schoen-G heat exchanger reduces along the streamwise direction of SCO2, but it slightly rises in PCHE. This effect may be due to heat transfer enhancement by vortices located in the sharpened corners in PCHE.

The temperature difference ΔT_s between SCO2 and the metal sheet decreases vastly toward the outlet in PCHE, especially in the regions: $z/\Delta z = 0$–$0.3(T_1 = 45$℃$)$, 0–$0.48(T_1 = 40$℃$)$, 0–$0.50(T_1 = 32.5$℃$)$. This phenomenon may be associated with the development of the vortex shown in Fig. 6. The temperature difference in TPMS Schoen-G heat exchanger shows less variation streamwise and lower than in PCHE, particularly in the regions: $z/\Delta z = 0$–$0.3(T_1 = 45$℃$)$, 0–$0.48(T_1 = 40$℃$)$, 0–$0.50(T_1 = 32.5$℃$)$. Beyond those regions, the temperature difference

in the former is higher than or comparable to the latter at $T_1 = 45$℃ or $T_1 = 40$, 32.5℃. This fact shows that the TPMS Schoen-G heat exchanger is more effective in heat transfer at lower inlet temperature/Reynolds number.

The temperature contour and streamline in the two heat exchangers at $p_1 = 9$ MPa are quite similar as those in Fig. 5 and Fig. 6, thus they are no longer present. The reason for the increased friction factor at $p_1 = 9$ MPa shown in Fig. 9 (a) is attributed to the enlarged dynamic viscosity from $p_1 = 8$ MPa to $p_1 = 9$ MPa.

3.2. The thermal performance

The mean heat transfer coefficient U of SCO2 in the hot side of TPMS Schoen-G heat exchanger and PCHE is plotted in Fig. 8 (a) as a function of the mean bulk temperature T_b at the inlet pressure $p_1 = 8$ MPa, 9 MPa. The peaks in U are found themselves near the pseudocritical points but on their right due to nonuniform temperature distribution streamwise. The peaks in U at $p_1 = 9$ MPa are lower than at $p_1 = 8$ MPa. These effects
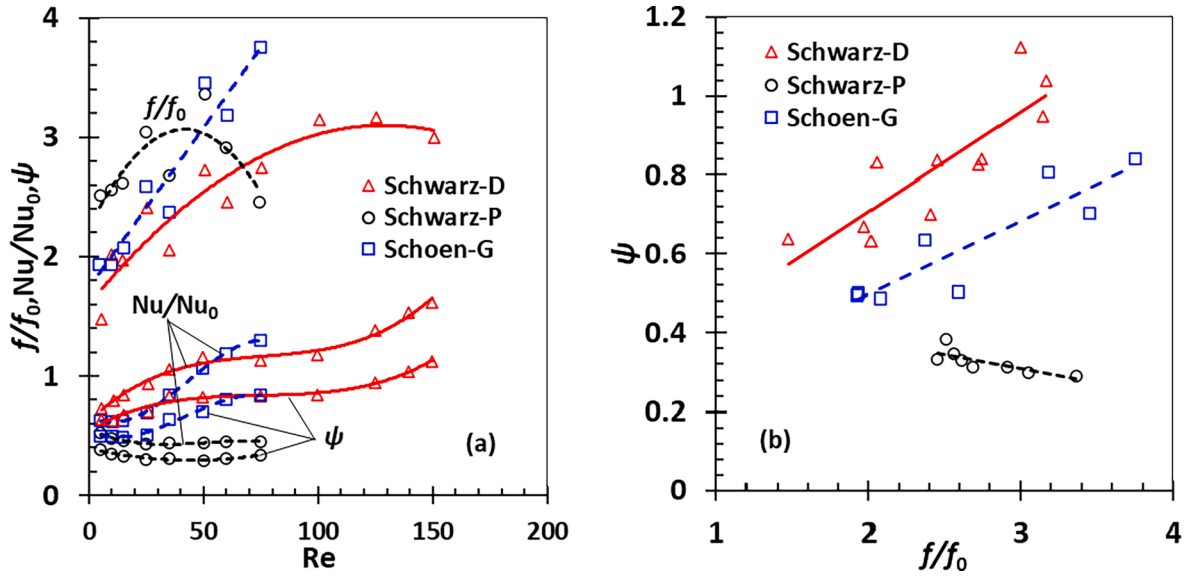
Fig. 11. Thermal and hydraulic performance parameters f/f_0, Nu/Nu$_0$, ψ of the counter-flow heat exchanger with core structure of TPMS in laminar flow regime, the plots are generated based on the raw data in Ref. [12].
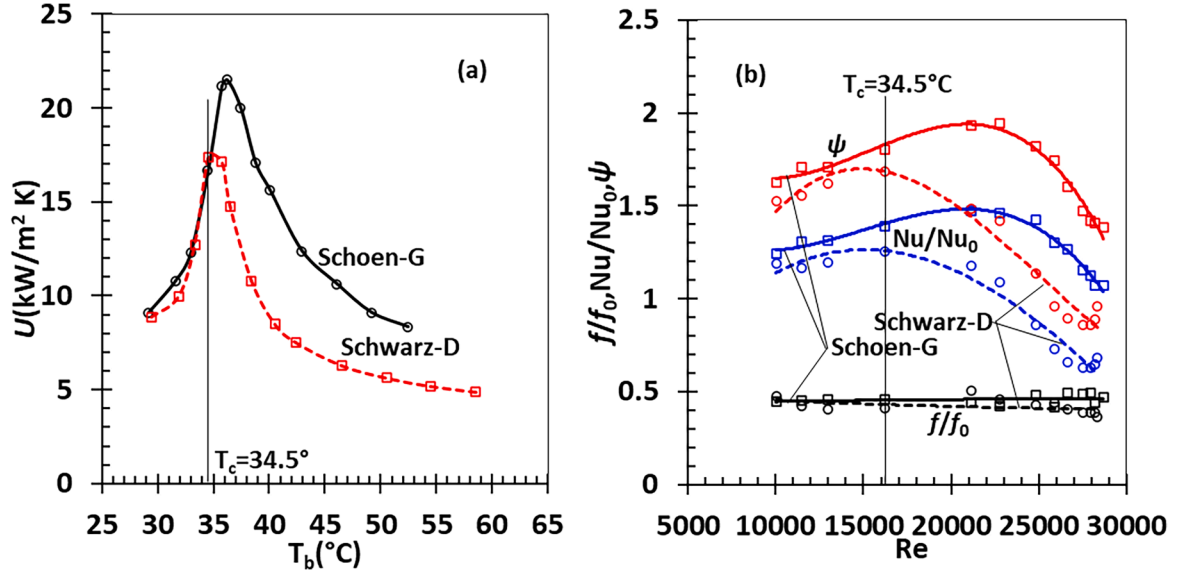
Fig. 12. Mean heat transfer coefficient U, the ratios f/f_0, Nu/Nu$_0$ and ψ curves of TPMS Schoen-G and Schwarz-D heat exchangers, (a)U, (b) three ratios.

are the same as those presented in Ref. [23].

Based on the mean bulk specific heat capacity at constant pressure C_{pb}, dynamic viscosity μ_b and λ_b, the SCO2 Prandtl number $Pr(=C_{pb}\mu_b/\lambda_b)$, which is the ratio of kinematic viscosity to thermal diffusivity, can be calculated, and are demonstrated in Fig. 8 (b). Obviously, the peaks in U are attributed to the peaks in the Pr curves.

The mean heat transfer coefficient U of TPMS Schoen-G heat exchanger is larger than PCHE at the same mean bulk temperature and inlet pressure. This fact suggests that heat transfer enhancement exists in TPMS Schoen-G heat exchanger compared with PCHE.

The friction factors f, f_0 and Nusselt numbers Nu, Nu_0 of TPMS Schoen-G heat exchanger and PCHE are demonstrated in Fig. 9 at $p_1 = 8$ MPa, 9 MPa. It is clear that the friction factor of TPMS Schoen-G heat exchanger is lower than PCHE, but the Nusselt number of TPMS Schoen-G heat exchanger is larger than PCHE at the same inlet pressure. When the inlet pressure rises to 9 MPa from 8 MPa, the friction factor rises but Nusselt number declines for both heat exchangers.

3.3. The heat transfer enhancement

To exactly assess the heat transfer enhancement, the friction factor ratio f/f_0, Nusselt number ratio Nu/Nu_0 and PEC ψ are plotted in Fig. 10 (a) when the Reynolds number Re varies at $p_1 = 8$ MPa, 9 MPa. The friction factor ratio f/f_0, Nusselt number ratio Nu/Nu_0 and PEC ψ are in the ranges of 0.38–0.50, 1.07–1.49, and 1.45–2.04, depending on both Re and T_1. The friction factor ratio f/f_0 shows less variation with Re. Based on ψ values, the best heat transfer enhancement is achieved in Re $= 15,000$–$25,000$. As Re $> 25,000$, the ψ values drop off quickly. When Re is lower than 15,000, the ψ values decrease steadily but slowly with reducing Re. The Nusselt number ratio Nu/Nu_0 exhibits a similar trend with Re as PEC ψ. Generally, the heat transfer enhancement at $p_1 = 9$ MPa is better than that at $p_1 = 8$ MPa as Re $< 25,000$, or slightly poorer when Re $> 25,000$ in terms of the ψ values.

This phenomenon may be attributed to Pr profiles of TPMS shown in Fig. 10 (b). The Pr value at $p_1 = 9$ MPa is much lower than that at $p_1 = 8$
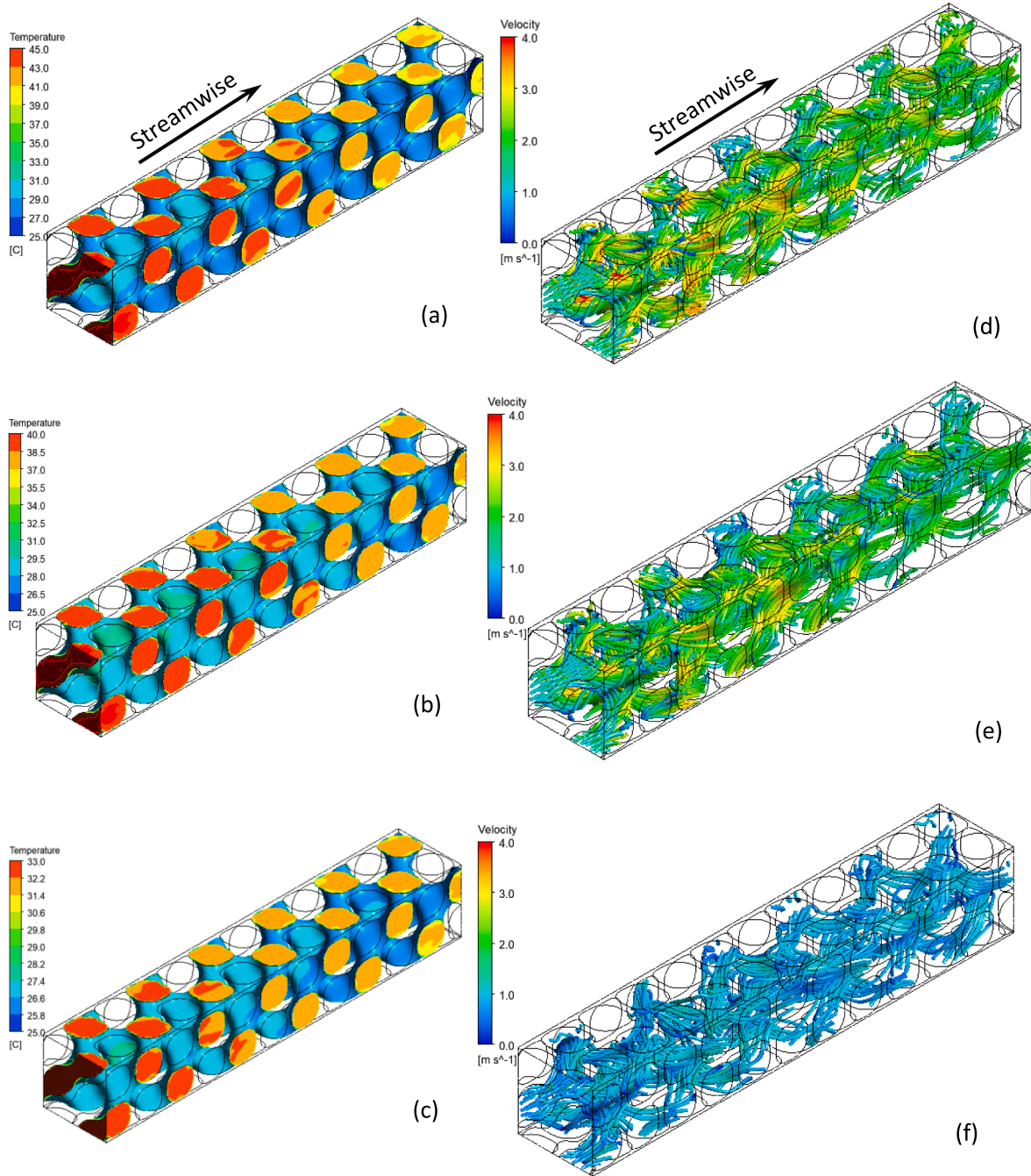
Fig. 13. SCO2 temperature contour and streamline in TPMS Schwarz-D heat exchanger at $T_1 = 45, 40, 32.5$℃, $p_1 = 8$ MPa, (a)-(c) temperature, (d)-(f) streamline, (a) & (d) for $T_1 = 45$℃, (b) & (e) for $T_1 = 40$℃, (c) & (f) for $T_1 = 32.5$℃.

MPa, while the dynamic viscosity varies a little as the inlet pressure rises from 8 MPa to 9 MPa. This fact suggests that heat diffusion in boundary layer is more dominant than momentum diffusion at $p_1 = 9$ MPa, thus small *Pr* value at $p_1 = 9$ MPa may be responsible for the better Nusselt number ratio Nu/Nu_0 and PEC ψ as Re $< 25,000$ compared with the ratio and PEC at $p_1 = 8$ MPa.

4. Discussion

In the paper, the counter-flow conjugated heat transfer in TPMS Schoen-G heat exchanger and PCHE, in which they share the same hydraulic diameter, was investigated with CFD simulations when SCO2 inlet temperature varied across the pseudocritical point, but the inlet

temperature and flow rate of cold water remained unchanged. The heat transfer enhancement of the TPMS Schoen-G heat exchanger was assessed when the PCHE served as a reference heat exchanger. The effect of SCO2 inlet pressure on the enhancement was identified as the inlet pressure was at 8 MPa and 9 MPa. This sort of study hasn't been available in the literature. The results in the paper are meaningful to the design and selection of water-cooled counter-flow heat exchanger in the cooling or cold storage system with SCO2 as a working medium.

Based on ψ values predicted with CFD simulations, heat transfer enhancement of the TPMS Schwarz-D heat exchangers is better than the TPMS Schoen-G heat exchangers when the flow is laminar at Re < 150 [12] or turbulent at Re $< 20,000$ [15]. The thermal and hydraulic performance parameters, f/f_0, Nu/Nu_0 and ψ, are compiled and shown in
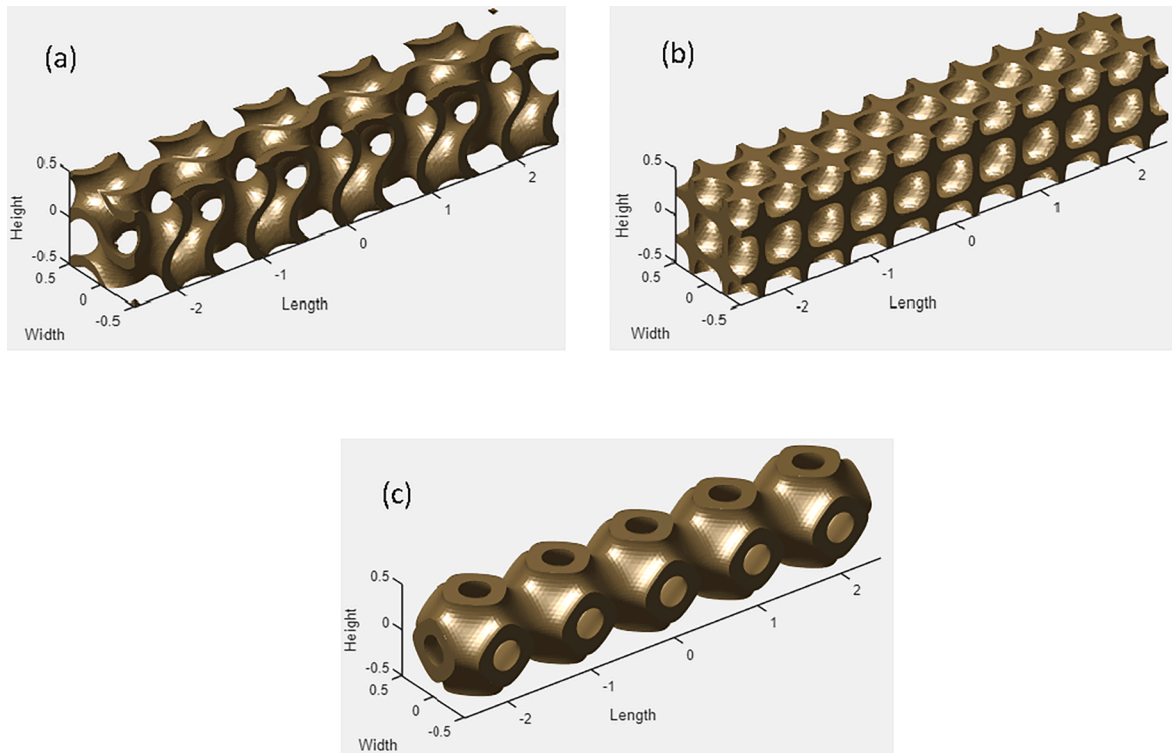
Fig. 14. Typical examples of TPMS Schoen-G, Schwarz-D and Schwarz-P structures, (a) Schoen-G, (b) Schwarz-D, (c) Schwarz-P, one TPMS cell is plotted in the width and the heigh directions, but five cells in the length direction, the structures were created with MSLattice.

Table 4
Material and geometrical parameter of the PCHE model.

Component	Parameter	Type	Value
Solid plate	Material	SS316L	
	Thickness(mm)	1.63	
	Thermal conductivity (W/m K)	16.3	
Fluid channel	Diameter(mm)	Hot	1.9
		Cold	1.8
	Depth(mm)	Hot	0.95
		Cold	0.9
	Longitudinal pitch (mm)	Hot	4.5
		Cold	3.62
	Zigzag angle (°)	Hot	115
		Cold	100
	Gap of between two channels (mm)	Hot	0.6
		Cold	0.7

Fig. 11 based on the raw data in Ref. [12]. Here f and Nu are the friction factor and Nusselt number of the heat exchanger with TPMS core structure of Schwarz-P or Schwarz-D or Schoen-G, f_0 and Nu_0 are the friction factor and Nusselt number of the reference heat exchanger with a smooth tube. According to the figures, the f/f_0 and Nu/Nu_0 values rise with increasing Re in the cases of Schwarz-D and Schoen-G. ψ ascends with increasing f/f_0 in the two cases. Based on the f/f_0-ψ plot, Schwarz-D seems to be the best in heat transfer enhancement compared with Schwarz-P and Schoen-G in laminar flow regime.

The conjugated heat transfer in the TPMS Schwarz-D heat exchanger adopted in Ref. [15] was simulated under the conditions: G=355 kg/ m²s, p_1=8MPa, T_1=65-30°C to compare the thermal and hydraulic performance of the TPMS Schoen-G heat exchanger in turbulent regime. The mean heat transfer coefficient U, f/f_0, Nu/Nu_0 and ψ curves are present in Fig. 12. The reference heat exchanger is the PCHE. The U value of the TPMS Schwarz-D heat exchanger is lower than the TPMS Schoen-G heat exchanger, especially at the pseudocritical point and on its right where a near 50 % reduction is seen. Even though the ratio f/f_0

of the TPMS Schwarz-D heat exchanger is smaller than the TPMS Schoen-G heat exchanger, the ratio Nu/Nu_0 of the former is poorer than the latter, particularly at the pseudocritical point and on its right. The ψ value is significantly degraded at the pseudocritical point and on its right but shows a slight increase on the left of the point. This proves that the heat transfer enhancement of the TPMS Schwarz-D heat exchanger maybe equivalent to or better than the TPMS Schoen-G heat exchanger at Re < 15,000. This outcome agrees with that in Ref. [15].

The SCO2 temperature contour and streamline in the TPMS Schwarz-D heat exchanger at p_1 = 8 MPa, T_1=45, 40, 32.5°C are illustrated in Fig. 13. The temperature decreases steadily downstream. However, the temperature near the sheet wall seems to be lower at T_1 = 45°C than at the other temperatures, suggesting a poorer heat transfer condition at a higher inlet temperature. This phenomenon is related to a smaller U shown in Fig. 12 as $T_1 > T_c$.

The flow channels in the TPMS Schwarz-D heat exchanger are multi-connection, and perpendicular to each other. The fluid streams smoothly from one channel to another without any noticeable separation but with twist. However, high velocity zones are observed when the SCO2 experiences variation in velocity orientation at T_1 = 45, 40°C.

The areas of heat transfer surface are 2.213, 3.115 and 3.762 cm² for PCHE, TPMS Schoen-G and Schwarz-D heat exchangers with the same hydraulic diameter and streamwise length, respectively. This means that SCO2 particles must travel in longer paths through the TPMS Schoen-G and Schwarz-D heat exchangers than through the PCHE to enhance heat transfer. The mechanism of heat transfer enhancement in TPMS heat exchangers is attributed to a larger heat transfer surface area and more topological tortuosity without flow separation.

The temperature, pressure drops, and friction factor in hot and cold channels are validated based on a partial-length (54 mm) PCHE model against the experimental data in Refs. [24,25], CFD simulated data on the full length PCHE model [26] and the partial-length (120 mm) PCHE model [27], respectively. The detail about the validation is referred to Appendix B. It is shown that the errors in temperature and pressure drops are 15 % in the hot channels, while the errors in temperature drop
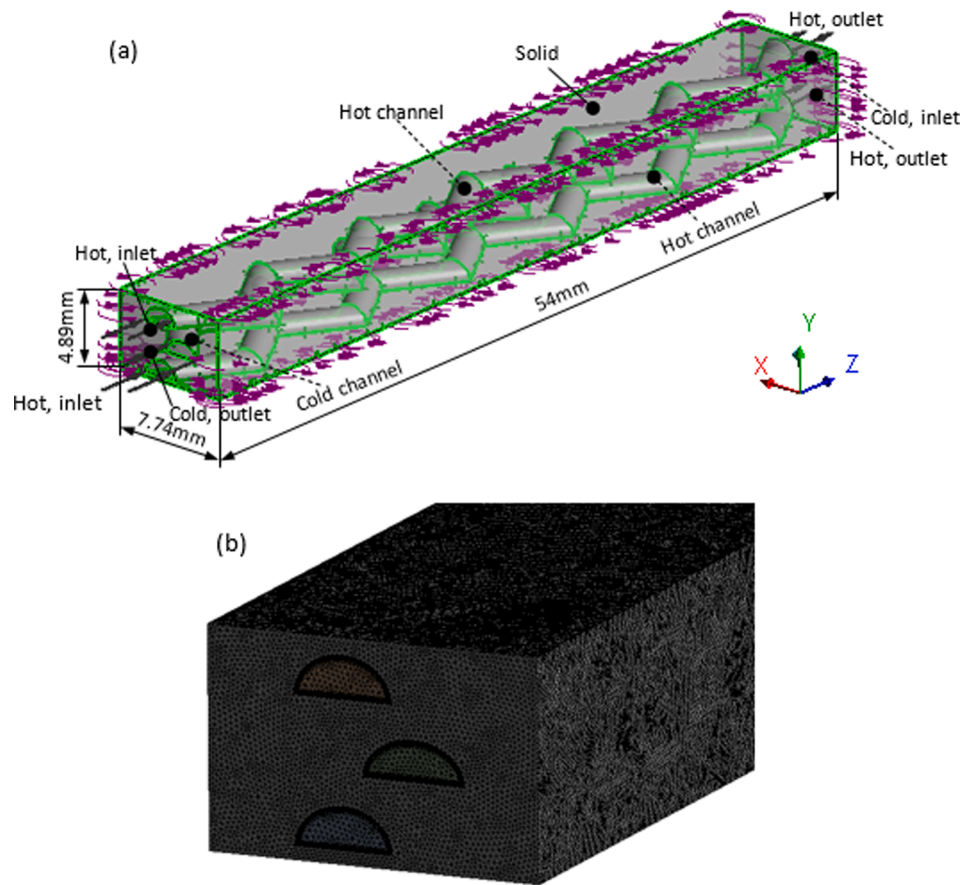
Fig. 15. Fluid and solid domains of the PCHE model used in [27,36], the PCHE is originated from Ref. [24], (a)fluid and solid domains, (b) mesh generated, the curved arrows indicate translational periodical boundary condition for a pair of two opposite surfaces in the solid domain.

Table 5
Boundary conditions at inlet and outlet of the PCHE model.

Hot channels Experimental data in [24]			Cold channel interpolated with curves in [26] predicted by CFD		Experimental data in [24]
p_1(kPa)	T_1(K)	m_f(kg/s)	p_1(kPa)	T_1(K)	m_f(kg/s)
2545.5	552.9	1.445×10^{-4}	8283.81	494	3.152×10^{-4}

and pressure drop are 0.6 % and 10.4 %, respectively. The errors in friction factor varies in a range of (33.8–37.6)% in the hot channels, and (0.6–22.4)% in the cold channel compared with the factors predicted with empirical correlations in Refs. [24,25,27] This is because the structured mesh with better accuracy was used in Refs. [26,27], while the tetrahedral dominant mesh is adopted here. Further, the partial-length of the PCHE model is 54 mm, thus the higher wall shear stress in the entrance length may make a larger contribution to the pressure drop than the wall shear stress in a longer PCHE model.

Nevertheless, there are a couple of limitations in the present study. First, in these simulations, SCO2 mass flux was different from TPMS Schoen-G heat exchanger to PCHE to allow the inlet Reynolds number of SCO2 to be nearly identical in two heat exchangers at the same inlet temperature. Second, the mass flow rate and inlet temperature of cold water were kept constant in the simulations, consequently, the mean heat flux from the hot SCO2 to the cold water varied from one SCO2 inlet temperature to another. It is very difficult to maintain a constant mean heat flux by adjusting the inlet temperature and mass flow rate of the cold water in a conjugated heat transfer simulation [23]. Third, the

Table 6
Information on the meshes employed in CFD simulations of SCO2 in the PCHE model.

Geometrical model		PCHE model of 7.74(width) × 4.89 (height) × 54(length)mm		
Mesh name		Mesh7		Mesh8
Element size(mm)		0.125		0.11
Nodes		1,780,410		2,352,258
Elements	Total	5,734,317		7,604,727
	Tet4	3,616,993(63.1 %)		4,825,123 (63.4 %)
	Wed6	2,117,324(36.9 %)		2,779,604 (36.6 %)
Element quality		0.5762 ± 0.3513		0.5845 ± 0.3418
Aspect ratio		11.12 ± 19.06		9.75 ± 16.42
Skewness		0.2314 ± 0.1386		0.2282 ± 0.1370
Orthogonal quality		0.7664 ± 0.1392		0.7702 ± 0.1368
Channel		Cold	Hot	Cold	Hot
Inflation mesh for boundary layer	First layer height (mm)	0.00125	0.0025	0.00125	0.0025
	Number of layers	14	14	14	14
	Growth rate	1.2	1.2	1.2	1.2
	y^+	1.11	0.94	1.08	0.96

predicted thermal and hydraulic performance of two TPMS heat exchangers are not confirmed with experimental data, because there are no such experimental data of TPMS heat exchangers in turbulent regime. Hopefully, the experimental data can be provided in our laboratory supported by new funding available in the future. Four, the experimental PCHE in Ref. [25], which was selected as a simulated PCHE in Ref. [15], has sharp zigzag channels. Therefore, this geometrical model has to be kept in use here. Even though this kind of zigzag channels

Table 7
Errors of temperature and pressure drops across hot and cold channels at two sets of mesh.

Channel	Mesh	ΔT_s(K) CFD	ΔT_s(K) Exp	Error (%)	Δp(Pa) CFD	Δp(Pa) Exp	Error (%)
Hot	Mesh7	30.76	26.78	14.9	2090	1765	18.4
	Mesh8	30.79		15.0	2030		15.0
Hot	Mesh7	30.83		15.1	2180		23.5
	Mesh8	30.94		15.5	2060		16.7
Cold	Mesh7	25.96	25.82	0.5	8080	6250	29.3
	Mesh8	25.99		0.6	6900		10.4

$\Delta T_s = T_{s1} - T_{s2}$ for hot channels, $\Delta T_s = T_{s2} - T_{s1}$ for cold channel, $\Delta p = p_1 - p_2$ for hot and cold channels, error=(CFD-Exp) × 100 %/Exp, the experimental inlet temperature T_{s1} and pressure p_1 for cold channel, outlet temperature T_{s2} and pressure p_2 for hot channels were interpolated with the curves predicted by CFD [26].

Table 8
Comparison of the errors in temperature, pressure drops and friction factors with those in the literature.

Turbulence model	Channel	Error in ΔT_s (%)	Error in Δp (%)	Re	f
SST, present	Hot	15.0	15.0	4,709	0.205
	Cold	0.6	10.4	11,414	0.370
k-ε, present	Hot	7.8	−21.2	4,642	0.142
	Cold	−0.2	−14.2	11,132	0.304
k-ε in [26]	Hot	−2.4	1.8	N/A	
	Cold	0.5	−10.7		
SST in [27]	Hot	2.3	3.6	4709	0.153
	Cold	1.3	3.6	11,414	0.339
Correlation in [24]	Hot	N/A		4709	0.149
	Cold			11,414	0.368
Correlation in [25]	Hot	N/A		4709	0.153
	Cold			11,414	0.302
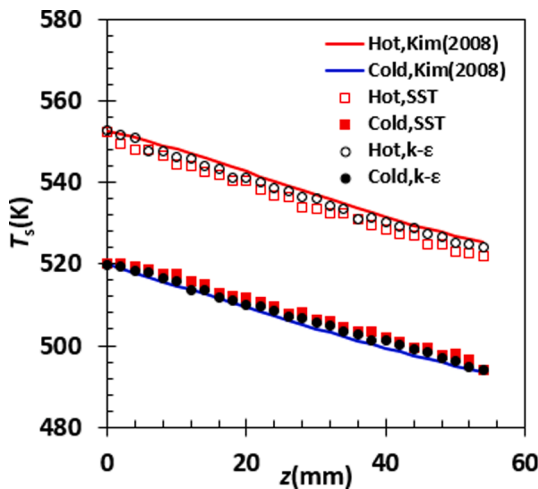
Fig. 16. Temperature streamwise profiles in the hot and cold channels based on the full- and partial-length PCHE models, the lines stand for the profiles predicted with the k-ε turbulence model on the full-length (846 mm) PCHE [26], the symbols show the profiles calculated on the partial-length (54 mm)PCHE model here.

suffers from significant flow resistance but gains the best Nusselt number, its thermal and hydraulic performance is still steadily improved by using CFD [28–31] and analytical method [32]. However, novel studies on PCHE with smooth/blunt zigzag channels emerged to make a proper trade-off between flow resistance and Nusselt number, for example, the curvature of the fillet in zigzag channels was optimized in [33–35] by using CFD and [36] by analytical approach. The zigzag channels with

flat fillet and wavy shapes were simulated with CFD method [37]. The sinusoidal fin-based PCHE was proposed and simulated by using CFD [38] and the PCHE with C-shaped channels were developed and optimized by employing analytical method [39]. The results achieved in the paper are not applicable to PCHEs with smooth/blunt zigzag channels. Heat transfer enhancement of TPMS heat exchangers against PCHEs with smooth/blunt zigzag channels is desirable in the future. Finally, the buoyancy effect of SCO2 in the two heat exchangers was not taken into account here, this issue should be clarified in further work.

The aim of this paper is focused on the thermal and hydraulic of TPMS heat exchanger only, thus its fabrication is not mentioned. Usually, TPMS heat exchangers are fabricated by using 3D printing technique. This fact suggests that TPMS heat exchangers may be more expensive than PCHEs. However, a TPMS heat exchanger is subject to more effective heat transfer and lower flow resistance than a PCHE does, hence the operational cost of TPMS heat exchangers can be less than that of PCHEs. Obviously, a techno-economic analysis should be performed to decide which heat exchanger is the best for the cooling or cold storage system with SCO2 as a working medium in the future.

The TPMS heat exchanger simulated here is for the cooling or cold storage system with SCO2 as a working medium. The operational pressure of the system is around (8–9) MPa rather than a pressure of 100 MPa or more in the SCO2 thermal power system. Whether the TPMS heat exchanger can bear a pressure in (8–9) MPa needs confirmation by performing a finite element analysis on the structure of the TPMS heat exchanger in the future.

5. Conclusions

The conjugated heat transfer of SCO2 in TPMS Schoen-G heat exchanger and PCHE was simulated under counter-flow conditions when SCO2 inlet temperature varied in 65–30 °C and the inlet pressure is at 8 MPa, 9 MPa but cold-water inlet temperature and mass flow rate remained constant. The thermal and hydraulic performance of two heat exchangers were obtained, and heat transfer enhancement of the TPMS Schoen-G heat exchanger was evaluated when the PCHE served as a reference heat exchanger. The SCO2 temperature contours, streamlines, cross-sectional averaged temperature streamwise profile and streamwise profile of temperature difference between SCO2 and metal sheet were illustrated and discussed. It turned out that the mean heat transfer coefficient of TPMS Schoen-G heat exchanger is higher than PCHE at the same inlet temperature and inlet pressure of SCO2. When the inlet pressure rises, the friction factor increases and Nusselt number decreases in both heat exchangers, but the PEC gets better. The friction factor ratio f/f_0, Nusselt number ratio Nu/Nu_0 and PEC ψ depend on both Reynolds and inlet temperature and are ranged in 0.38–0.50, 1.07–1.49, and 1.45–2.04. The temperature of SCO2 decreases downstream in two heat exchangers, especially for TPMS Schoen-G heat exchanger at a higher inlet temperature. The cross-sectional averaged temperature difference in TPMS Schoen-G heat exchanger varies less in the streamwise direction and is smaller than in PCHE, especially in the regions: $z/\Delta z$=0–0.3(T_1 = 45 °C), 0–0.48(T_1 = 40 °C), 0–0.50(T_1 = 32.5 °C). Otherwise, the temperature difference in the former is larger than or comparable to the latter at T_1 = 45 °C or T_1 = 40, 32.5°C. The streamlines in TPMS Schoen-G heat exchanger are considerably smooth toward downstream even though a higher velocity appears in the areas with greater curvature. The streamlines near the wall are trapped in each corner in PCHE and spiral flow patterns are generated to lead to a significant hydraulic loss but heat transfer enhancement. In comparison with TPMS Schwarz-D heat exchanger, TPMS Schoen-G heat exchanger exhibits much better heat transfer enhancement at a Reynolds number >16,000. The TPMS Schoen-G heat exchanger potentially can be used as a SCO2 cooler in cooling or cold storage systems when SCO2 serves as a working medium from the thermal and hydraulic performance point of view. The fabrication of the heat exchanger and experiment on it will be the next issue for us.

Declaration of Competing Interest

The authors declare that they have no known competing financial interests or personal relationships that could have appeared to influence the work reported in this paper.

Data availability

Data will be made available on request.

Appendix A. . Triply periodic minimal surfaces and applications

.

A.1. Triply periodic minimal surfaces

Minimal surfaces are one kind of surfaces with a zero-mean curvature at any point on them. Minimal surfaces are infinite, periodic and intersection-free in three-dimensional (3D) Euclidean space, and called triply periodic minimal surface (TPMS) and can be traced back to as early as 1865 presented by H A Schwarz [40]. There are about 45 sorts of minimal surfaces presently, but Schoen-Gyroid(G), Schwarz-Diamond(D) and Schwarz-Primitive(P) are the most meaningful minimal surfaces to engineering. The shape of these minimal surfaces is described mathematically by using the following equations [41]:

$$\begin{cases} \sin x \cos y + \sin y \cos z + \sin z \cos x = c, \text{Schoen} - \text{G} \\ \cos x \cos y \cos z - \sin x \sin y \sin z = c, \text{Schwarz} - \text{D} \\ \cos x + \cos y + \cos z = c, \text{Schwarz} - \text{P} \end{cases} \tag{17}$$

where x, y, z are the Cartesian coordinates of a minimal surface, c is a constant, two different values in c can make a minimal surface become TPMS structure with thickness, i.e., TPMS metal sheet. There are a couple of free software for generating TPMS structures, for example, Minisurf in Ref. [42] and MSLattice in Ref. [41]. Typical examples of TPMS Schoen-G, Schwarz-D and Schwarz-P structures are demonstrated in Fig. 14. Since TPMS structures are complex, they are usually fabricated by employing additive manufacturing or 3D printing techniques.

A.2. Applications of TPMS structures

A.2.1. Static mixers
Four TPMS static mixers such as Schoen-G, Schwarz-D, Schoen-IWP, and Schwarz-P types were studied by using computational fluid dynamics (CFD), the dimensionless power number and the coefficient of variance were employed to quantify the energy consumption and mixing efficiency of the mixers. For single element mixers, three TPMS mixers consume less energy and with a comparable or better mixing efficiency than the Kenics mixer. For multiple element mixers, however, the Kenics mixer has a better mixing efficiency but less energy consumption than the TPMS mixers [2].

A.3. Mass transfer packing

An improved structured packing heat and mass transfer device based on TPMS and TPMS skeletons wherein the skeletons are hollow and used as conduits for heating and cooling fluids was proposed. Two preferred examples include the TPMS and skeleton of Schwarz-D surface and the TPMS and skeleton of Schoen-G surface [3]. TPMS structures are potentially applied to CO2 capture by building multifunctional, intensified devices. Three typical TPMS structures, namely, Schoen-G, Schwarz-D, and Schwarz-P, were investigated by using CFD to simulate the counter-current flows of CO2 binding organic liquids (CO2BOL) solvent in the TPMS structures. Two sizes of unit cell were tested in each type of TPMS. A preliminary understanding of the TPMS structure behaviours in counter-flow conditions was provided [43]. Mass transfer simulations through the LaNi5 metal hydride packing with TPMS Schoen-G structure were carried out in COMSOL Multiphysics, and an improved adsorption performance was observed by using TPMS metal hydride packing compared with traditional tank design [44]. TPMS was used in feed channel spacer in membrane distillation application to enhance water mass flux and heat transfer coefficient. The 60 % higher water flux and 63 % larger overall film heat transfer coefficient were achieved by the TPMS spacers than the commercial spacer [45].

A.5. Heatsinks

Heat sinks with architected networks such as TPMS Schoen-G sheet, Schoen-G solid, and Schwarz-D solid, were made by 3D printing technique. Moreover, functionally graded heat sinks were also designed, and their flow and heat transfer characteristics were investigated using CFD simulation. Uniform heat sinks with Schoen-G sheet-networks had the highest convective heat transfer coefficient but the highest pressure drop due to their largest surface area and topological tortuosity. The heatsink with increasing porosity along the flow direction resulted in reduced pressure drop and convective heat transfer coefficient. However, the pressure drop outweighed the convective heat transfer coefficient reduction [4].

A.6. TPMS porous media

The Stokes flow and fluid permeability through six different TPMS porous media such as Schwartz-P, Schwartz-D, and Schoen-G minimal surfaces, two different pore-channel models, and a simple cubic array of spherical obstacles (benchmark model) were numerically determined by using the

immersed-boundary finite-volume method. It was found that the Schwartz-P porous medium has the highest fluid permeability in the six triply periodic porous media considered at the porosity 0.5 [5]. Porous media were designed by using TPMS, based on the mathematically defined Schoen-IWP, Schwarz-P, Schwarz-D and Schoen-G surfaces, and morphological analysis of the media was conducted to characterise the porous structure of the media. TPMS porous structures: Schoen-IWP (0.0014–0.8994), Schwarz-P (0.0192–0.7160), Schwarz-D (0.0048–0.8515), and Schoen-G (0.0078–0.9728). It was demonstrated that Schwarz-P structure had the smallest flow resistance and highest comprehensive heat transfer coefficient. The TPMS porous structure showed better thermal and hydraulic performance and stronger structural strength [46]. The effects of 3D printing on pressure drop of TPMS structured packing (porous media) were studied numerically and experimentally and multi-jet fusion 3D printing results in the lowest pressure drop across the packing samples than stereolithography and selective laser sintering techniques [47].

A.7. Scaffolds in tissue engineering

A scaffold architecture with sheetlike morphology based on TPMS is with significant structural and mechanical advantages over conventional designs. These porous solid structures have better mechanical stiffness than conventional network solids. The scaffolds with Schoen-G, Schwarz-D and Schwarz-P structures were designed, fabricated, simulated by using finite element method (FEM) in software Abaqus, the modulus of TPMS unit cell, TPMS scaffold and cubic unit cell was tested [48]. Scaffold designs with network solid or sheet solid of TPMS Schoen-G were derived. Against conventional network solids, sheet solids are with favourable mechanical properties and larger specific surface area [49]. Femur bone scaffold, iliac bone scaffold, and spine bone scaffold were designed by using hybrid method of distance field and TPMS structure unit cell. Biomimetic scaffolds were designed by using TPMS Schoen-IWP, Schwarz-P structures. The mechanical behaviour of these structures was predicted with FEM in software Abaqus. The effect of thickness and surface radius on porosity and mechanical behaviour was clarified [50]. Scaffolds with TPMS Schwarz-D and Schwarz-P were designed, their mechanical properties and deformation were predicted and tested, the effect of stress concentration was discussed [51]. Scaffolds with TPMS structures were designed, simulated with FEM and tested under compression, suitable TPMS structures with proper permeability and mechanical properties were obtained [52]. Scaffolds with Schwarz-D, Schwarz-P and Schoen-G structures were designed and fabricated, their mechanical behaviour was tested and simulated under compression, the TPMS Schoen-G structure is a better choice for biomimetic scaffolds [53]. Interestingly, the anisotropic elastic property of five TPMS structures for scaffolds was investigated with FEM [54], the mechanical behaviour of skeletal-TPMS lattices of Schwarz-D, Schwarz-P, Schoen-G and Schoen-IWP was analysed and compared with that of strut-TPMS lattices [55].

Since the distance field algorithm was applied to the Boolean operations of the anatomical model and TPMS structure unit cells, almost defect-free porous scaffolds with complicated micro-structure and high-quality external surfaces can be easily obtained [56]. The sigmoid function method and Gaussian radial basis function method were proposed to design TPMS-based structures with given transition boundaries for functionally graded porous structures in tissue engineering [57]. A review of the design methods for complex topology structures, including scaffolds with TPMS elements, fabricated by using additive manufacturing methods was unfolded [58].

To be honest, scaffolds with TPMS structure have drawn significant attention, and are experiencing rapid development presently, an exhausting review of this topic is out of the scope of the paper.

Appendix B. Validation of Temperature, pressure drops and friction factor in PCHE

The SCO2 experimental temperature and pressure drops across the hot and cold channels of a zigzag PCHE published in [24] were employed to validate the standard k-ε two-equation turbulence model by using a full-length geometrical model, i.e. 7.74(width) $\times$ 4.89(height) $\times$ 846(length)mm with three channels (one code channel and two hot channels) [26]. The error in temperature drop across the cold channel was as small as 0.51 % but the error in pressure drop across that channel was lower by 10.7 % than the experimental pressure drop when the SCO2 inlet temperature, outlet pressure and mass flow rate were specified as the boundary conditions in CFD code-Fluent 6.3 [26]. The predicted streamwise pressure and temperature profiles in the cold and hot channels were provided. Recently, a partial-length geometrical model of that PCHE such as 7.74(width) $\times$ 4.89 (height) $\times$ 120(length)mm was used to validate the SST turbulence model [27,36] to adapt computational resources available. The pressure and temperature interpolated at 120 mm by using the streamwise pressure and temperature in the cold channels predicted in Ref. [26] was adopted as the boundary conditions while the interpolated pressure and temperature interpolated at 120 mm in the hot channels were employed to calculate the pressure and temperature drops. This method is selected here, but the length of the PCHE is cut off at 54 mm because of our limited computing resources. The physical and geometrical parameters of plate and flow channels of the PCHE model is listed in Table 4. The corresponding fluid and solid domains and mesh structure of the PCHE model generated in ANSYS DesignModeler are illustrated in Fig. 15.

The governing equations and turbulence model of SCO2 flowing in the PCHE model and numerical methods for solving the equations are identical to those in Section 2.2. The known inlet pressure and temperature as well as SCO2 mass flow rate are present in Table 5. These pressure and temperatures were specified in the inlet of the hot and cold channels, while the mass flow was given in the outlet of the channels. Two pairs of outside surfaces of the solid domain shown in Fig. 15 were used as solid–solid translational periodical boundary conditions. Three solid–fluid interfaces were set up between the hot, cold channels and the solid domain. The rest two surfaces of the solid domain were adiabatic.

Two sets of mesh, i.e., Mesh7 and Mesh8 were generated in ANSYS meshing module to examine mesh size effect on pressure and temperature drops across the hot, cold channels. Their information is tabulated in Table 6. The y^+ values of these meshes are around 1 and satisfactory. The errors in temperature and pressure drops across the hot and cold channels against the experimental data are listed in Table 7. It is shown that the errors in temperature drop across the hot and cold channels vary a little from Mesh7 to Mesh8. However, the error in pressure drops across the hot and cold channel change greatly, and the pressure drops at Mesh8 are subject to the smaller errors, namely 15 % in temperature and pressure drops in the hot channels, 0.6 % in temperature drop and 10 % in pressure drop in the cold channel. Thus, Mesh8 is adopted in the CFD simulations.

The errors in temperature, pressure drops and friction factor estimated in the present paper are compared with those determined by empirical correlations based on experimental or CFD simulated data in the literature in Table 8. The results calculated with the k-ε turbulence model are included in the table as well. There are two types of friction factor: one is Fanning friction factor, and the other one is Darcy–Weisbach friction factor. The Darcy–Weisbach friction factor is equal to four times the Fanning friction factor in value at the same Reynolds number in a pipe. The Fanning friction factor is defined as the ratio of the local wall shear stress to the local flow kinetic energy density and has been used by chemical engineers. The Fanning friction factor occurs most frequently in the literature on PCHEs with a few expectations such as [32,36]. The Darcy–Weisbach friction factor,

see Eq. (15), is more popular in mechanical engineering than the Fanning friction factor, thus The Darcy–Weisbach friction factor is adopted in this paper.

Based on the CFD results in Ref. [27], the empirical correlations of the Darcy–Weisbach friction factor f for the hot and cold channels in the zigzag PCHE are written as:

$$f = \begin{cases} 4 \times 0.1108 \mathrm{Re}^{-0.126}, \text{hot channel} \\ 4 \times 0.1859 \mathrm{Re}^{-0.084}, \text{cold channel} \end{cases} \tag{18}$$

$$f = \begin{cases} 4 \times \left(0.0467 - 2 \times 10^{-6}\mathrm{Re}\right), \text{hot channel} \\ 4 \times \left(0.1013 - 2 \times 10^{-6}\mathrm{Re}\right), \text{cold channel} \end{cases} \tag{19}$$

and.

$$f = \begin{cases} 4 \times \left(0.04495 - 1.402 \times 10^{-6}\mathrm{Re}\right), \text{hot channel} \\ 4 \times \left(0.09318 - 1.545 \times 10^{-6}\mathrm{Re}\right), \text{cold channel} \end{cases} \tag{20}$$

Eqs. (18)-(20) are employed to calculate the Darcy–Weisbach friction factors in the last three rows in Table 8.

The error in ΔT_s across the cold channel estimated with the SST turbulence model the present paper is as good as those predicted with the k-ε model [26] and SST model [27]. The error in Δp across the cold channel given by the SST in the present paper is better than that provided with the k-ε model [26] but poorer than that with the SST model [27]. The errors in ΔT_s and Δp across the hot channels estimated with the SST model here are larger than the errors in Refs. [26,27]. The reason is that the structured mesh in Refs. [26,27] may have better accuracy than the tetrahedral dominant mesh used due to the lack of ICEM software here. Additionally, since the length of the PCHE model is as short as 54 mm, the higher wall shear stress in the entrance length may attribute a more significant contribution to the pressure drop than the wall shear stress in a longer PCHE model does. The k-ε model can produce a smaller ΔT_s but a larger error in Δp.

The friction factor f in the hot channels predicted with the SST model here is higher by 33.8 %, 37.6 %, and 34.4 % compared to those predicted with Eqs. (18)-(20). The factor in the cold channel is larger by 22.4 %, 0.6 %, and 9.0 % than the factors estimated by Eqs. (18)-(20). The friction factor f in the hot channels predicted with the k-ε model here is smaller by -7.4 %, -4.9 %, and -6.9 % than those predicted with Eqs. (18)-(20). The factor in the cold channel is lower by 0.0 %, -17.4 %, and -10.6 % than the factors given by Eqs. (18)-(20). This fact suggests that the k-ε model can underestimate the pressure drop in a zigzag PCHE model.

The temperature streamwise profiles in the hot and cold channels predicted with the SST and k-ε model based on the full-length (846 mm) PCHE model in Ref. [26] and partial-length (54 mm) PCHE model here are illustrated in Fig. 16. The k-ε model results in very similar temperature profiles in the hot and cold channels on both the PCHE models. The temperature profile in the hot channels predicted with the SST model is lower than the profile calculated with the k-ε model, causing a larger ΔT_s, then a greater error in ΔT_s is resulted here.

References

[1] I. Kaur, P. Singh, State-of-the-art in heat exchanger additive manufacturing, Int. J. Heat Mass Transf. 178 (2021), 121600, https://doi.org/10.1016/j.ijheatmasstransfer.2021.121600.

[2] M. Ouda, O. Al-Ketan, N. Sreedhar, M. I. Hasan Ali, E. K. Abu Al-Rub, S. K. Hong, H. A. Arafat, Novel static mixers based on triply periodic minimal surface (TPMS) architectures, Journal of Environmental Chemical Engineering 8(2020) 104289. 10.1016/j.jece.2020.104289.

[3] R. C. Ryan, Minimal surface area mass and heat transfer packing, US2014/0014493A1, USA, 2014. https://patents.google.com/patent/US20140014493A1/en.

[4] O. Al-Ketan, M. Ali, M. Khalil,R. Rowshan, K. A. Khan, R. K. Abu Al-Rub, Forced convection computational fluid dynamics analysis of architected and three dimensional printable heat sinks based on triply periodic minimal surfaces, ASME Journal Thermal Science and Engineering Applications 13(2021) 021010. 10.1115/1.4047385.

[5] Y. Jung, S. Torquato, Fluid permeabilities of triply periodic minimal surfaces, Physical Review E 72(2005) 056319. https://journals.aps.org/pre/pdf/10.1103/PhysRevE.72.056319.

[6] Z. Dong, X. Zhao, Application of TPMS structure in bone regeneration, Engineered Regeneration 2 (2021) 154–162, https://doi.org/10.1016/j.engreg.2021.09.004.

[7] V. B. Slaughter, Method of using minimal surfaces and minimal skeletons to make heat exchanger components, US7866377B2, USA, 2011. https://patents.google.com/patent/US7866377B2/en.

[8] T. Femmer, A.J.C. Kuehne, M. Wessling, Estimation of the structure dependent performance of 3-D rapid prototyped membranes, Chem. Eng. J. 273 (2015) 438–445, https://doi.org/10.1016/j.cej.2015.03.029.

[9] D.T. Nguyen, P. Roy, V.A. Beck, J.K. Stolaroff, Triply periodic minimal surface heat exchangers for supercritical CO2 cycles. In: Proceedings of 14th International Conference on Greenhouse Gas Control Technology, 2018.

[10] G. Chandrasekaran, 3D printed heat exchangers: An experimental study, Master thesis, Arizona State University, Tempe, USA, 2018.

[11] H. Peng, F. Gao and W. Hu, Design, modeling and characterization of triply periodic minimal surface heat exchangers with additive manufacturing, In: Proceedings of the 30th Annual International Solid Freeform Fabrication Symposium–An Additive Manufacturing Conference, Austin, USA, 2019. https://repositories.lib.utexas.edu/bitstream/handle/2152/90564/2019-194-Peng.pdf?sequence=2&isAllowed=y.

[12] A. G. P. Passos, Laminar flow and heat transfer in triply periodic minimal surfaces, Master thesis, Tecnico Lisboa, Lisboa, Portugal, 2019. https://fenix.tecnico.ulisboa.pt/downloadFile/1126295043836646/ThesisAndrePassos.pdf.

[13] I. Wadsö, S. Holmqvist, Additively manufactured heat exchangers: Development and testing, Master thesis, Lund University, Lund, Sweden, 2020.

[14] B. W. Reynolds, Simulation of flow and heat transfer in 3d printable triply periodic minimal surface heat exchangers, PhD thesis, University of Canterbury, Christchurch, New Zealand, 2020. https://ir.canterbury.ac.nz/handle/10092/102500.

[15] W. Li, G. Yu, Z. Yu, Bioinspired heat exchangers based on triply periodic minimal surfaces for supercritical CO2 cycles, Appl. Therm. Eng. 179 (2020), 115686, https://doi.org/10.1016/j.applthermaleng.2020.115686.

[16] J. Kim, D.J. Yoo, 3D printed compact heat exchangers with mathematically defined core structures, J. Comput. Des. Eng. 7 (2020) 527–550, https://doi.org/10.1093/jcde/qwaa032.

[17] T. Dixit, E. Al-Hajri, M.C. Manosh, P. Nithiarasu, S. Kumar, High performance, microarchitected, compact heat exchanger enabled by 3D printing, Appl. Therm. Eng. 210 (2022), 118339, https://doi.org/10.1016/j.applthermaleng.2022.118339.

[18] K. Kuwahara, S. Higashiiue, D. Ito, S. Koyama, Experimental study on cooling heat transfer of supercritical carbon dioxide inside horizontal micro-fin tubes, Transactions of Japan Society of Refrigerating and Air Conditioning Engineers 24 (2007) 173-181. 10.11322/tjsrae.24.173.

[19] H.S. Lee, H.J. Kim, J.I. Yoon, K.H. Choi, C.H. Son, The cooling heat transfer characteristics of the supercritical CO2 in micro-fin tube, Heat Mass Transfer 49 (2013) 173–184.

[20] Ansys, ansys,, CFX-Solver Theory Guide, ANSYS Inc, Canonsburg, 2011.

[21] F. Menter, J.C. Ferreira, T. Esch, B. Konno, The SST turbulence model with improved wall treatment for heat transfer predictions in gas turbines. In: Proceedings of the International Gas Turbine Congress, 2003.

[22] B.A. Kader, Temperature and concentration profiles in fully turbulent boundary layers, Int. J. Heat Mass Transf. 24 (1981) 1541–1544, https://doi.org/10.1016/0017-9310(81)90220-9.

[23] W. Li, Z. Yu, Y.Y. Wang, Y. Li, Heat transfer of supercritical carbon dioxide in a tube-in-tube heat exchanger-a CFD study, The Journal of Supercritical Fluids 181 (2022), 105493, https://doi.org/10.1016/j.supflu.2021.105493.

[24] T. Ishizuka, Y. Kato, Y. Muto, K. Nikitin, N. L. Tri and H. Hashimoto, Thermal–hydraulic characteristic of a printed circuit heat exchanger in a supercritical CO2 loop, In: The 11th International Topical Meeting on Nuclear Reactor Thermal-Hydraulics (NURETH-11), Avignon, France, 2005.

[25] K. Nikitin, Y. Kato, L. Ngo, Printed circuit heat exchanger thermal–hydraulic performance in supercritical CO2 experimental loop, Int. J. Refrig. 29 (2006) 807–814, https://doi.org/10.1016/j.ijrefrig.2005.11.005.

[26] D.E. Kim, M.H. Kim, J.E. Cha, S.O. Kim, Numerical investigation on thermal–hydraulic performance of new printed circuit heat exchanger model, Nucl.

Eng. Des. 238 (2008) 3269–3276, https://doi.org/10.1016/j.nucengdes.2008.08.002.

[27] M. Saeed, M.H. Kim, Thermal and hydraulic performance of SCO2 PCHE with different fin configurations, Appl. Therm. Eng. 127 (2017) 975–985, https://doi.org/10.1016/j.applthermaleng.2017.08.113.

[28] H.H. Khan, A.M. Aneesh, A. Sharma, A. Srivastava, P. Chaudhuri, Thermal-hydraulic characteristics and performance of 3D wavy channel based printed circuit heat exchanger, Appl. Therm. Eng. 87 (2015) 519–528, https://doi.org/10.1016/j.applthermaleng.2015.04.077.

[29] A. Meshram, S.D. Khivsara, J.D. Ortega, C. Ho, R. Bapat, P. Dutta, Modeling and analysis of a printed circuit heat exchanger for supercritical CO2 power cycle applications, Appl. Therm. Eng. 109 (2016) 861–870, https://doi.org/10.1016/j.applthermaleng.2016.05.033.

[30] M. Saeed, A.A. Awais, A.S. Berrouk, CFD aided design and analysis of a precooler with zigzag channels for supercritical CO2 power cycle, Energy Convers. Manage. 236 (2021), 114029, https://doi.org/10.1016/j.enconman.2021.114029.

[31] M. Saeed, A.S. Berrouk, M.S. Siddiqui, A.A. Awais, Numerical investigation of thermal and hydraulic characteristics of sCO2-water printed circuit heat exchangers with zigzag channels, Energy Convers. Manage. 224 (2020), 113375, https://doi.org/10.1016/j.enconman.2020.113375.

[32] Y. Yang, H. Li, M. Yao, Y. Zhang, C. Zhang, Optimizing the size of a printed circuit heat exchanger by multi-objective genetic algorithm, Appl. Therm. Eng. 167 (2020), 114811, https://doi.org/10.1016/j.applthermaleng.2019.114811.

[33] S.M. Lee, K.Y. Kim, S.W. Kim, Multi-objective optimization of a double-faced type printed circuit heat exchanger, Appl. Therm. Eng. 60 (2013) 44–50, https://doi.org/10.1016/j.applthermaleng.2013.06.039.

[34] S. Baik, S.G. Kim, J. Lee, J.I. Lee, Study on CO2–water printed circuit heat exchanger performance operating under various CO_2 phases for S-CO_2 power cycle application, Appl. Therm. Eng. 113 (2017) 1536–1546, https://doi.org/10.1016/j.applthermaleng.2016.11.132.

[35] S.J. Yoon, J. O'Brien, M. Chen, P. Sabharwall, X. Sun, Development and validation of Nusselt number and friction factor correlations for laminar flow in semi-circular zigzag channel of printed circuit heat exchanger, Appl. Therm. Eng. 123 (2017) 1327–1344, https://doi.org/10.1016/j.applthermaleng.2017.05.135.

[36] K. Bennett, Y.T. Chen, Printed circuit heat exchanger performance analysis using non-uniform segmental design method, Appl. Therm. Eng. 153 (2019) 69–84, https://doi.org/10.1016/j.applthermaleng.2019.02.102.

[37] S.Y. Lee, B.G. Park, J.T. Chung, Numerical studies on thermal hydraulic performance of zigzag-type printed circuit heat exchanger with inserted straight channels, Appl. Therm. Eng. 123 (2017) 1434–1443, https://doi.org/10.1016/j.applthermaleng.2017.05.198.

[38] M. Saeed, M.H. Kim, Thermal-hydraulic analysis of sinusoidal fin-based printed circuit heat exchangers for supercritical CO2 Brayton cycle, Energy Convers. Manage. 193 (2019) 124–139, https://doi.org/10.1016/j.enconman.2019.04.058.

[39] M. Saeed, A.S. Berrouk, M.S. Siddiqui, A.A. Awais, Effect of printed circuit heat exchanger's different designs on the performance of supercritical carbon dioxide Brayton cycle, Appl. Therm. Eng. 179 (2020), 115758, https://doi.org/10.1016/j.applthermaleng.2020.115758.

[40] A. H. Schoen, Infinite Periodic Minimal Surfaces Without Self-Intersection, NASA TN D-5541, Cambridge, USA, 1970. https://ntrs.nasa.gov/citations/19700020472.

[41] O. Al-Ketan and R. K. Abu Al-Rub, MSLattice: A free software for generating uniform and graded lattices based on triply periodic minimal surfaces, Material Design & Processing Communications 3(2021) e205. 10.1002/mdp2.205.

[42] M.T. Hsieh, L. Valdevit, Minisurf–A minimal surface generator for finite element modeling and additive manufacturing, Software Impacts 6 (2020), 100026, https://doi.org/10.1016/j.simpa.2020.100026.

[43] Y. Fu, Z. Xu, G. Panagakos, CFD study of countercurrent flow in triply periodic minimal surfaces with CO2BOL solvent, Pacific Northwest National Laboratory, Richland, USA, 2019 https://www.osti.gov/biblio/1691506-cfd-study-countercurrent-flow-triply-periodic-minimal-surfaces-co2bol-solvent.

[44] L.A. Lesmana, M. Aziz, Triply periodic minimal surface-based heat exchanger as metal hydride hydrogen storage reactor, Chemical, Engineering Transactions 88 (2021) 229–234, https://doi.org/10.3303/CET2188038.

[45] N. Thomas, N. Sreedhar, O. Al-Ketan, R. Rowshan, R. K. Abu Al-Rub, H.Arafat, 3D printed triply periodic minimal surfaces as spacers for enhanced heat and mass transfer in membrane distillation, Desalination 443(2018) 256-271. 10.1016/j.desal.2018.06.009.

[46] Z. Cheng, R. Xu, P.X. Jiang, Morphology, flow and heat transfer in triply periodic minimal surface based porous structures, Int. J. Heat Mass Transf. 170 (2021), 120902, https://doi.org/10.1016/j.ijheatmasstransfer.2021.120902.

[47] A. Zimmer, J. D. Pacheco Araujo, K. A. Andreassen, C. A. Grande, Effect of manufacturing techniques in pressure drop on triple periodical minimal surface packings, Chemie Ingenieur Technik 93(2021) 967-973. 10.1002/cite.202000237.

[48] S. Rajagopalan, R.A. Robb, Schwarz meets Schwann: Design and fabrication of biomorphic and durataxic tissue engineering scaffolds, Med. Image Anal. 10 (2006) 693–712, https://doi.org/10.1016/j.media.2006.06.001.

[49] S.C. Kapfer, S.T. Hyde, K. Mecke, C.H. Arns, G.E. Schröder-Turk, Minimal surface scaffold designs for tissue engineering, Biomaterials 32 (2011) 6875–6882, https://doi.org/10.1016/j.biomaterials.2011.06.012.

[50] H.A. Almeida, P.J. Bártolo, Design of tissue engineering scaffolds based on hyperbolic surfaces: Structural numerical evaluation, Med. Eng. Phys. 36 (2014) 1033–1040, https://doi.org/10.1016/j.medengphy.2014.05.006.

[51] J. Kadkhodapour, H. Montazerian, S. Raeisi, Investigating internal architecture effect in plastic deformation and failure for TPMS-based scaffolds using simulation methods and experimental procedure, Mater. Sci. Eng., C 43 (2014) 587–597, https://doi.org/10.1016/j.msec.2014.07.047.

[52] H. Montazerian, E. Davoodi, M. Asadi-Eydivand, J. Kadkhodapour, M. Solati-Hashjin, Porous scaffold internal architecture design based on a minimal surface: A compromise between permeability and elastic properties, Mater. Des. 126 (2017) 98–114, https://doi.org/10.1016/j.matdes.2017.04.009.

[53] A.P.G. Castro, J. Santos, T. Pires, P.R. Fernandes, Micromechanical Behavior of TPMS Scaffolds for Bone Tissue Engineering, Macromol. Mater. Eng. 305 (2020) 2000487, https://doi.org/10.1002/mame.202000487.

[54] Y. Lu, W. Zhao, Z. Cui, H. Zhu, C. Wu, The anisotropic elastic behavior of the widely-used triply-periodic minimal surface based scaffolds, J. Mech. Behav. Biomed. Mater. 99 (2019) 56–65, https://doi.org/10.1016/j.jmbbm.2019.07.012.

[55] X. Guo, X. Zheng, Y. Yang, X. Yang, Y. Yi, Mechanical behavior of TPMS based scaffolds: A comparison between minimal surfaces and their lattice structures, SN Applied Sciences 1 (2019) 1145, https://doi.org/10.1007/s42452-019-1167-z.

[56] D.J. Yoo, Porous scaffold design using the distance field and triply periodic minimal surface models, Biomaterials 32 (2011) 7741–7754, https://doi.org/10.1016/j.biomaterials.2011.07.019.

[57] N. Yang, Z. Quan, D. Zhang, Y. Tian, Multi-morphology transition hybridization CAD design of minimal surface porous structures for use in tissue engineering, Comput. Aided Des. 56 (2014) 11–21, https://doi.org/10.1016/j.cad.2014.06.006.

[58] J. Feng, J. Fu, Z. Lin, C. Shang, B. Li, A review of the design methods of complex topology structures for 3D printing, Visual Comput. Industry, Biomed. Art 1 (2018) 5, https://doi.org/10.1186/s42492-018-0004-3.